Waste and Biomass Valorization (2025) 16:333–355
https://doi.org/10.1007/s12649-024-02651-9

ORIGINAL PAPER

Roles of $Ce_{1-x}Zr_xO_2$/SBA-15 in Selective Catalytic Glycerol Conversion to Lactic Acid Process: Process Behaviors and Kinetic Analyses

Syamima Nasrin Mohamed Saleh[1] · **Fakhrony Sholahudin Rohman**[1] · **Anwar Ul-Hamid**[2] · **Ahmad Zuhairi Abdullah**[1]

Received: 30 March 2024 / Accepted: 3 July 2024 / Published online: 25 July 2024

Abstract

The surge in glycerol production from the oleochemical industry prompted the aggressive search for new value-added derivatives such as lactic acid. A series of novel $Ce_{1-x}Zr_xO_2$ catalysts on mesoporous SBA-15 were synthesized and tested in a 50 mL reactor for up to 2 h for oxidative lactic acid synthesis from glycerol. A suitable kinetic model to represent the reaction was identified and kinetic parameters were calculated. The $10Ce_{1-x}Zr_xO_2$/SBA-15 catalyst, at a 15 wt% catalyst-to-glycerol ratio, exhibited impressive activity, achieving 94.2% glycerol conversion and 45.3% lactic acid yield at 260 °C. The reaction model shows good agreement with experimental data across various reaction conditions (R^2 values between 0.90 and 1.00). Based on a pseudo-second-order kinetic model, the selective conversion of glycerol to lactic acid was found to have an activation energy of 165.3 kJ/mol, with a high R^2 value of 0.94 which was lower than some reported results.

Graphical abstract

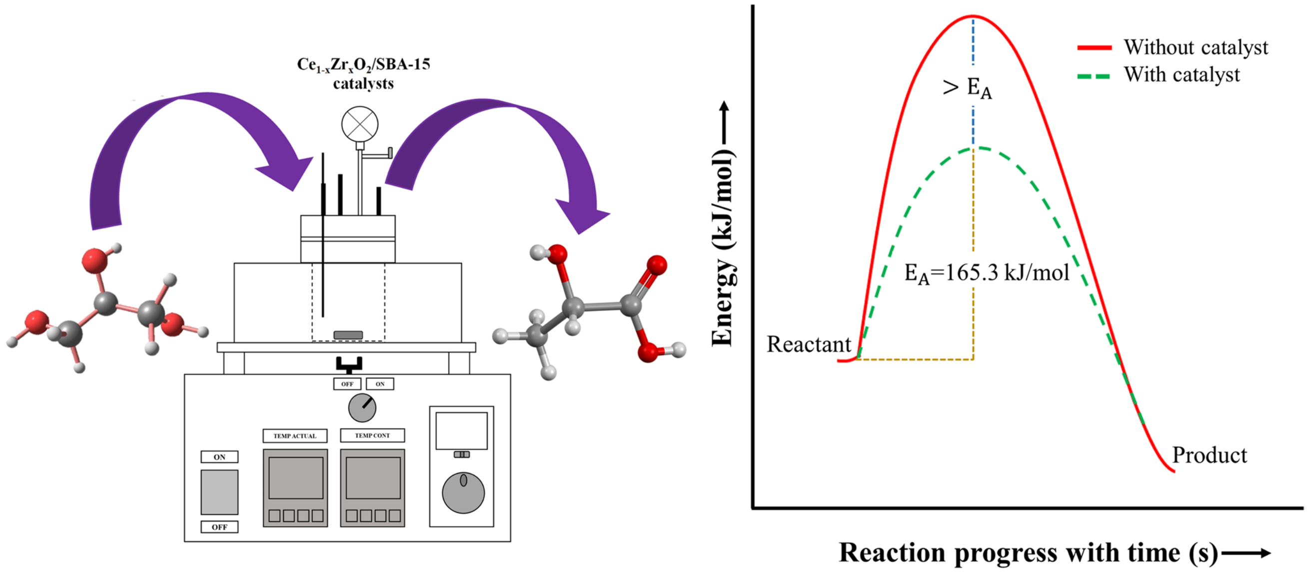

Keywords Selective glycerol conversion · Glycerol to lactic acid · Ordered mesoporous catalyst · Synergistic roles · Process model · Reaction kinetics

Statement of Novelty

The research described in the abstract fills a critical gap in the realm of sustainable chemical production. With the escalating production of glycerol as a byproduct of the booming

---

Extended author information available on the last page of the article

oleochemical industry, there arises an urgent need to address the associated environmental and economic challenges. Traditional disposal methods for excess glycerol are not only inefficient but also contribute to environmental pollution. By focusing on the conversion of glycerol into value-added chemicals like lactic acid, this research offers a compelling solution to this pressing issue. Lactic acid is a versatile compound with a wide range of industrial applications, including biodegradable polymers, pharmaceuticals, and food additives. Therefore, the development of efficient processes for lactic acid synthesis from glycerol not only adds value to a waste stream but also reduces reliance on fossil resources, promoting a more sustainable and circular economy. Additionally, the exploration of novel catalyst formulations and the development of kinetic models deepen our understanding of the underlying chemical processes, paving the way for further advancements in catalysis and process optimization. In essence, this research addresses a multifaceted need by tackling environmental concerns, promoting resource efficiency, and advancing scientific knowledge, thereby making a significant contribution to the field of chemical engineering.

Introduction

The increasing production of biodiesel through transesterification has led to a concurrent rise in glycerol generation, typically constituting between 10 and 14% of biodiesel by weight [1]. However, due to its comparatively lower commercial value, there is an immediate need for a more viable technological alternative to efficiently utilize glycerol. Glycerol has garnered significant research attention due to its potential for conversion into valuable chemicals, including 1,1-propanol [2], 1,2-propanediol [2], 1,3-propanediol [2], acrolein [3, 4], acrylic acid [4–6], and lactic acid [7–16]. Among these products, lactic acid stands out as it has numerous potential applications not only in the realm of organic chemistry but also extends its reach into diverse fields such as bioplastics, pharmaceuticals, cosmetics, detergent, etc. [17, 18].

Early investigations on a homogeneous glycerol-to-lactic acid transformation system were done using alkaline hydroxides such as KOH and NaOH per se and consistently promising results were demonstrated, with lactic acid yields ranging from 84 to 90% even at high glycerol conversions [8–10, 19]. Following that, research diverged into exploring colloidal metals as heterogeneous catalysts. The reason is that metal-based catalysts, in general, are inert in the reactor system and have additional benefits like good thermal stability, selection towards desired product, and environmental friendliness. In general, copper [11, 16, 20–22], platinum [12], nickel [13], palladium [14, 23], and trimetallic particles supported on metal oxides [15] have been widely studied. Overall, these supported metal-based catalysts exhibited excellent catalytic performance, achieving lactic acid selectivities ranging from 60% to 95.4% at glycerol conversions exceeding 90% [24]. It is noteworthy that the studies have proven that in most chemical reactions, especially in lactic acid synthesis, multi-metallic catalysts, which include two or more different metal species, offer several advantages over single-atom catalysts. These advantages result from the metals' distinctive synergistic interactions, which can increase catalytic activity and selectivity.

In actuality, the complex tandem reaction of selective glycerol-to-lactic acid conversion capitalizes on the synergistic effects of at least two proximate active sites, enhancing the efficiency of this reaction. The available literature is primarily focused on micro-level studies, specifically investigations into catalysts, catalyst components, activity, selectivity, stability, and reaction mechanisms, whereas macro-level studies that delve into engineering aspects such as process modeling and reaction kinetics are relatively scarce. To date, there have been no dedicated efforts to develop an empirical model capable of accurately predicting the glycerol conversion and lactic acid yield in glycerol-to-lactic acid oxidation reactions within the realm of process modeling. Much work remains to be done in this area; however, one of the persistent challenges is the lack of accurate characterization of the mass transfer parameters.

In early studies, Chen and his co-workers utilized a CaO catalyst to investigate the kinetics of glycerol-to-lactic acid conversion [7]. The study was conducted at various reaction temperatures (280–300 °C). A maximum glycerol conversion and a lactic acid yield of 92.4% and 72.9%, respectively, were achieved for the fed-batch conversion of crude glycerol. In this study, it was also concluded that lactic acid selectivity was highly dependent on the initial glycerol concentration, reaction temperature, and catalyst loading. The kinetic model for glycerol-to-lactic acid conversion under the applied conditions was reported to obey a first order concerning initial glycerol concentration, whereas the pre-exponential factor and activation energy reported were 6.154×10^{8} min^{-1} and 114 kJ/mol, respectively.

Apart from that, the same research group conducted a series of kinetic investigations to assess the glycerol-to-lactic acid transformation employing $Ni_{0.3}$/graphite [25], Cu/HAP [26], and Cu_{PEG} [11] catalysts. Their research demonstrated that all catalysts exhibited exceptional catalytic performance, achieving glycerol conversions exceeding 90% while maintaining lactic acid selectivities above 90%. The impact of reaction parameters, including concentrations of glycerol and NaOH, as well as the reaction temperature, on the rate of glycerol consumption, was examined using a power-function reaction kinetic. In their work, glycerol was reported to follow non-elementary rate law with values of 0.36, 0.49, and 0.41 for Cu(16)/HAP, Cu_{PEG}, and $Ni_{0.3}$/graphite catalysts, respectively. Whereas, for NaOH, using Cu(16)/HAP, Cu_{PEG}, and $Ni_{0.3}$/graphite catalysts gave values of 0.47, 1.04, and 0.91, respectively. This showed when Cu_{PEG} and $Ni_{0.3}$/graphite catalysts were used, the rate of NaOH consumption followed nearly first-order rate law. The Cu(16)/HAP, Cu_{PEG}, and $Ni_{0.3}$/graphite catalysts exhibited different overall reaction orders and activation energies, with values of 1.13 and 117.2 kJ/mol, 1.53 and 76.3 kJ/mol, and 1.32 and 69.2 kJ/mol, respectively.

Recently, power-function type reaction kinetic equations were employed to assess the effect of glycerol and NaOH concentrations, along with reaction temperature, on glycerol-to-lactic acid oxidation reaction using 10% CuO/AC catalyst [21]. The activation energy was determined to be 134.39 kJ/mol, which was way greater than the activation energy for reactions using only a CuO catalyst. This suggested that the CuO/AC catalyst was more sensitive to temperature changes than the CuO catalyst alone. Also, it was noteworthy that the CuO/AC catalyst produced a higher yield of lactic acid at elevated temperatures than that of the CuO catalyst per se.

Indeed, many reactions are not suitable to be expressed in a simple rate law, whether they are homogenous or heterogeneous. This is because complex rate expressions for some reactions cannot be accurately predicted by only temperature- and concentration-dependent rate expressions. Additionally, to date, there has been no study done on the development of empirical process models to accurately predict the process behavior of the catalytic conversion of glycerol to lactic acid. Hence, this work is dedicated to investigating the behaviors of a $Ce_{1-x}Zr_xO_2$ catalyst supported on mesoporous SBA-15 to gain a deeper understanding of its synergistic role in the glycerol-to-lactic acid oxidation reaction, including experimental investigations, process modeling, and kinetic analysis.

Experimental

Preparation of $Ce_{1-x}Zr_xO_2$/SBA-15 Catalysts

The general method of preparation used to synthesize the $Ce_{1-x}Zr_xO_2$/SBA-15 catalysts in our previous work [27] was also employed in this work. As in a typical SBA-15 synthesis procedure, 10 g of Pluronic P-123 was first dissolved in 70 g of 2 M HCL and 150 g of distilled water. The obtained mixture was subjected to a 16-h stirring at a medium stirring rate. Next, 20 g of TEOS was added by drops to the clear solution and left for 8 h of vigorous stirring at 55 °C. The resulting solution was then transferred to a hydrothermal autoclave reactor and aged for another 16 h under static conditions at 80 °C. Afterward, the solid product was filtered and washed with 800 mL of deionized water. Subsequently, the procedure was followed by drying the resulting white solid material at 60 °C for 24 h. The organic template was eventually removed via 8 h calcination at 550 °C at a ramping rate of 2 °C C/min.

In this work, $Ce_{1-x}Zr_xO_2$/SBA-15 catalysts with varying total metal loadings (5, 10, 20, 30, and 40 wt%) were synthesized by using appropriate amounts of $Ce(NO_3)_3.6H_2O$ and $ZrO(NO_3)_2.xH_2O$ precursors relative to both the pre-calculated total metal loadings and the amount of SBA-15 support material. For instance, to prepare a $5Ce_{1-x}Zr_xO_2$/SBA-15 catalyst, 0.23436 g and 0.06240 g of $Ce(NO_3)_3.6H_2O$ and $ZrO(NO_3)_2.xH_2O$, respectively were used. Before impregnation, the prepared SBA-15 support was subjected to drying for 1 h at 80 °C. The measured amounts of both $Ce(NO_3)_3.6H_2O$ and $ZrO(NO_3)_2.xH_2O$ were individually dissolved in 20 mL of ethanol. After that, 1.9 g of SBA-15 was added to the mixture of both precursors. The mixture was stirred until it produced a free-flowing solution. The resulting material was then treated with NaOH until it reached a pH of 9, after which it was stirred at 70 °C C for around 6–7 h. Next, to remove excess sodium ions, the mixture was washed with deionized water and dried for 1.5 h at 80 °C C followed by a rise in temperature to 110 °C C for another 18 h. The catalyst was then subjected to calcination at 500 °C C for 4 h with a ramping rate of 2 °C C/min. The resulting catalysts with different loadings are referred to as $yCe_{1-x}Zr_xO_2$/SBA-15, where x indicates the fraction of Zr and the remaining fraction of Ce in the mixed metal oxides, and *y* denotes the theoretical total weight percent of Ce and Zr metals in SBA-15 support.

Characterization of $Ce_{1-x}Zr_xO_2$/SBA-15 Catalysts

To investigate the surface characteristics of all the synthesized catalysts, N_2 physisorption analysis was carried out using Micromeritics ASAP 2020 equipment. Before the analysis, the samples were degassed ($P < 10^{-1}$ Pa) at 300 °C C for 6 h to remove any impurities present in the catalysts. Next, FESEM (Quanta FEG 450) was used to examine the appearance of the surface morphological structure of all the synthesized catalysts. To ascertain the presence of hexagonal arrays and straight pores within the mesoporous channels of SBA-15 support, as well as to elucidate the structural characteristics of all the synthesized catalysts across different metal loadings, TEM micrographs were acquired using Philips FEI CM 12 TEM. An EDX technique was also performed to identify the elemental composition present on the surfaces of all the synthesized catalysts using a Quanta FEG 450 FESEM. The specific chemical bonds within the SBA-15 and all the synthesized catalysts were obtained by FTIR analysis using Perkin-Elmer 2000 Spectrometer using the potassium bromide (KBr) pellet technique.

Catalytic Activity Test and Reaction Product Analysis

The synthesis of lactic acid from glycerol using $y\text{Ce}_{1-x}\text{Zr}_x\text{O}_2$/SBA-15 catalysts was carried out in a batch system using a 50 mL modified stainless steel reactor equipped with a stirrer. In a typical procedure, 15 g of 13.23 M glycerol was mixed with appropriate amounts of the catalyst concerning glycerol, and the reactor was tightened properly. Before starting the reaction, the reactor was flushed with O_2 for 10 min to remove any excess air or humidity present inside the system. Moreover, the purging also helped provide oxygen-rich conditions inside the reactor. Then, the reactor was set at the desired temperature (250 °C) and the mixture was stirred continuously at 300 rpm for 2 h. After 2 h, the reaction was stopped, and the reactor was immersed in an ice bath to terminate the reaction. Likewise, the same procedure was systematically replicated across a range of metal loadings (5–40 wt%), catalyst loadings (5–40 wt%), and temperatures (240–270 °C).

For product analysis, the reaction sample was centrifuged to separate the solid catalyst from the liquid mixture. Then, the sample was mixed with the appropriate amount of 0.5 M H_2SO_4 to adjust the sample to a pH of 3–4. When a basic catalyst is used, it could result in the formation of the desired product in its ionized form, which is lactate ions rather than lactic acid. To convert these ions into their non-ionized, acidic forms, the pH of the solution needs to be adjusted. The sample was then filtered through a 0.22 µm PTFE 13 mm syringe filter. Next, the sample for analysis was prepared by diluting the filtered sample with deionized water. The sample analyses were done using an Agilent 1260 Infinity high-performance liquid chromatography (HPLC) equipped with a refractive index detector (RID) in series. A SHODEX Sugar SH1011 (8.0 × 300 mm, 6 µm) was used as the separating HPLC column. An aqueous solution of 0.0005 M H_2SO_4 was used as the mobile phase. The flow rate of the mobile phase was 0.6 mL/min, the column temperature was maintained at 60 °C for both left and right, and the RID detector temperature was set at 29 °C. The catalysts were assessed for their catalytic activity based on the glycerol conversion and lactic acid yield; and their ability to promote selective reactions towards lactic acid.

Catalyst Reusability Study

In the reusability study, the most active catalyst was used since the catalyst showed the highest activity. For this study, the first cycle of reaction was performed using specific loading of the fresh catalyst concerning 15 g of glycerol. The reaction was carried out at the best reaction conditions. After the first reaction, the catalyst was recovered from the reaction mixture through centrifugation at 4400 rpm for 40 min, followed by washing with 25 mL of methanol to remove the reactant and product from the surface of the catalyst. The recovered catalyst was then washed with deionized water to remove the excess methanol. The washed catalyst was dried at 80 °C for 1.5 h followed by raising the temperature to 110 °C for another 18 h. After that, the activated catalyst was reused for the next cycle of reaction following the same reaction conditions. The spent catalyst of each cycle was characterized using surface analysis using N2 physisorption, SEM, and EDX analyses using the same procedures as discussed earlier. Finally, the physicochemical and morphological characteristics of the spent catalyst were compared to those of the fresh catalyst to observe the changes that occurred after each cycle.

Process Modeling and Kinetic Study

In this work, MATLAB was employed to facilitate the process of model development through numerical computation, data analysis, and algorithm development. The process model development and kinetics analysis of selective glycerol oxidation to lactic acid involved a comprehensive study of the catalyst exhibiting the highest catalytic activity. The experiment was carried out by varying the reaction temperatures between 240 and 270 °C at the best reaction conditions at different times.

Process Model of Selective Glycerol-to-Lactic Acid Oxidation Reaction

The numerical differentiation of glycerol conversion over time was performed using second-order forward finite divided difference (Eq. 1) and centered finite divided difference (Eq. 2) formulas as follows:

$$f'\left(x_i\right) = \frac{-f\left(x_{i+2}\right) + 4f\left(x_{i+1}\right) - 3f\left(x_i\right)}{2h} \tag{1}$$

$$f'\left(x_i\right) = \frac{f\left(x_{i+1}\right) - f\left(x_{i-1}\right)}{2h} \tag{2}$$

To establish the correlation between the rate of change of conversion over time (*dx/*dt) and the conversion (*x*), a curve fitting tool in MATLAB was utilized for performing non-linear regression. The most suitable model that best fitted the experimental data, based on $R2 > 0.8$ was chosen, and the corresponding constant parameters of the chosen model were listed in another tab. The constant parameters were fine-tuned by establishing a correlation with temperature using the curve fitting tool. This iterative process aimed to identify the most accurate constant values that accurately represented the relationship between the parameters and temperatures. An empirical model, represented as a function of temperature, was proposed.

$$P = f(T) \tag{3}$$

The developed model was simulated by applying the fourth-order Runge–Kutta method for numerical differentiation, using the MATLAB ODE solver (*ode45* function). The general equation for the fourth-order Runge–Kutta method is as follows:

$$y_{i+1} = y_i + \frac{1}{6}\left(k_1 + 2k_2 + 2k_3 + k_4\right) \tag{4}$$

where $k_1 = f\left(x_i, y_i\right)$, $k_2 = f\left(x_i + \frac{1}{2}h, y_i + \frac{1}{2}k_1 h\right)$, $k_3 = f\left(x_i + \frac{1}{2}h, y_i + \frac{1}{2}k_2 h\right)$, $k_4 = f\left(x_i + h, y_i + k_3 h\right)$.

A similar method was also repeated to develop an empirical model to correlate the yield as a function of temperature. The developed model was validated with experimental data, ensuring accuracy and reliability. The simulation results were compared with the data obtained from the experimental data and validated using the correlation coefficient, R^2. R^2 values generally evaluate the squared difference between the simulated model and the experimental data, with the actual data being the average of the measured data. The R^2 values indicate the degree of accuracy of the model in fitting the experimental data. The R2 value is given by:

$$R^2 = 1 - \frac{SSE_{model}}{SSE_{total}} \tag{5}$$

where

$$SSE_{total} = \sum_{i-0}^{t} \left(x - \overline{x}\right)^2 \tag{6}$$

where x = Experimental data, $\overline{x}$ = Predicted data from the simulated model.

Kinetic Analysis of Selective Glycerol-to-Lactic Acid Oxidation Reaction

Meanwhile, the kinetic study was performed to identify the reaction rate constant (*ks*), activation energy (*Ea*), and pre-exponential factor (*A*) of this reaction. Lastly, a kinetic model was proposed to represent the selective glycerol oxidation reaction. Equation 8 was used to calculate the reaction rate constant (k) and several assumptions were made throughout the derivation of the rate Eq. (1) The reaction is irreversible. (2) The reaction involves mixed parallel and consecutive reactions. Hence, a pseudo-second-order reaction is assumed. (3) The reaction is carried out in a constant volume closed batch reactor. Thus, combining the mole balance, rate law, and reaction stoichiometry, the rate expression becomes:

$$\frac{dX}{dt} = kC_{Gly,initial}(1 - X)^2 \tag{7}$$

where k = Rate constant ($1/M.hr$), $C_{Gly,initial}$ = Initial concentration of glycerol (*mol/L*), X = Conversion of glycerol.

This equation was solved using MATLAB ODE solver (*ode45* function), followed by *fminsearch* function to estimate the k_s values for different temperatures (240–270 °C). Following the Arrhenius equation, the values of E_a and A were obtained using linear regression between ln$k$ versus $\frac{1}{T}$.

$$k = Ae^{-E_a/RT} \tag{8}$$

where A = Pre-exponential factor, E_a = Activation energy (*J/mol*), R = Universal gas constant (*8.3142 J/mol.K*), T = Temperature (*K*).

In addition, the kinetic model for the selective oxidation of glycerol into lactic acid was proposed, and the reliability of the model in predicting the glycerol conversion was validated based on the sum squared error (SSE) generated in MATLAB software. In general, SSE measures the deviations between the simulated and experimental data and is given by:

$$SSE = \sum_{i=0}^{t} \left(x - \overline{x}\right)^2 \tag{9}$$

where x = Experimental data, $\overline{x}$ = Predicted data from the simulated model.

Results and Discussion

Characterization of $Ce_{1-x}Zr_xO_2$/SBA-15 Catalysts

Physisorption Analysis

The surface and porosity analyses for SBA-15 support and all synthesized catalysts in different metal loadings (5 wt%, 10 wt%, 20 wt%, 30 wt%, and 40 wt%) were examined using N_2 physisorption analysis. The findings are presented in Table 1.

In general, the result in Table 1 indicates that the specific surface area decreased with increasing catalyst loadings. Moreover, the SBA-15 support, $5Ce_{1-x}Zr_xO_2$/SBA-15, $10Ce_{1-x}Zr_xO_2$/SBA-15, and $20Ce_{1-x}Zr_xO_2$/SBA-15 catalysts demonstrated a notably high specific surface area, falling within 419–529 m^2/g. However, it was worth noting that the $30Ce_{1-x}Zr_xO_2$/SBA-15 and $40Ce_{1-x}Zr_xO_2$/SBA-15 catalysts were observed to exhibit specific surface areas of 355 m^2/g and 297 m^2/g, respectively, which were lower than the typical range of specific surface areas exhibited by SBA-15 support.

Table 1 Surface and pore characteristics of SBA-15 support, *y*$Ce_{1-x}Zr_xO_2$/SBA-15, and spent $10Ce_{1-x}Zr_xO_2$/SBA-15 catalysts

Catalyst	Total surface area (m^2/g)[a]	Micropore area (m^2/g)[b]	External surface area (m^2/g)[b]	Micropore volume (cm^3/g)[b]	Total pore volume (cm^3/g)[c]	Average pore size (Å)[c]
SBA-15	678	248	429	0.1249	0.5970	51.47
$5Ce_{1-x}Zr_xO_2$/SBA-15	529	233	296	0.1179	0.4313	48.23
$10Ce_{1-x}Zr_xO_2$/SBA-15	503	184	276	0.0938	0.4068	51.33
$20Ce_{1-x}Zr_xO_2$/SBA-15	419	161	258	0.0821	0.3569	50.94
$30Ce_{1-x}Zr_xO_2$/SBA-15	355	148	207	0.0756	0.2843	45.48
$40Ce_{1-x}Zr_xO_2$/SBA-15	297	131	166	0.0671	0.2301	45.13
R1	351	40	301	0.0199	0.5823	58.92
R2	341	57	294	0.0284	0.6070	61.80
R3	312	41	271	0.0205	0.5757	64.54
R4	91	10	81	0.0047	0.3026	116.34

[a]from BET desorption method; [b]from t-plot method; [c]from BJH desorption method

Besides, with an increase in metal loadings, there was a possibility that the active $Ce_{1-x}Zr_xO_2$ compounds formed clusters or agglomerates that occupied the pores of SBA-15 support, causing pore blockage. Furthermore, at higher metal loadings, $Ce_{1-x}Zr_xO_2$ compounds had a higher tendency to aggregate and form separate CeO_2 and ZrO_2 metal phases rather than being evenly dispersed as a mixed oxide compound on SBA-15 support. This finding was also reported in previous studies conducted on various mixed metal oxide catalyst systems [28, 29]. Thus, all these reasons might have contributed to the reduction in available surface areas for catalysts with increasing metal loadings.

In addition, Table 1 illustrates that all synthesized catalysts exhibited average pore sizes that were nearly identical to that of SBA-15 support. This suggested that the SBA-15 support's mesoporous structure was well-preserved upon impregnation of $Ce_{1-x}Zr_xO_2$ compounds even at high metal loadings. Moreover, the average pore sizes decreased from 51.33 to 45.13 Å with increasing metal loadings from 10 to 40 wt% except for the $5Ce_{1-x}Zr_xO_2$/SBA-15 catalyst. This deviation from the general trend was potentially due to experimental errors during the catalyst synthesis procedure. Increasing metal loadings could result in the formation of more $Ce_{1-x}Zr_xO_2$ compounds on the SBA-15 support's surface. Consequently, this led to a reduction in average pore size as partial pore blockages occurred with greater frequency.

Furthermore, the micropore area, micropore volume, and total pore volume decreased as the metal loadings increased from 5 to 40 wt%. Also note that all three, micropore area, micropore volume, and total pore volume of all synthesized catalysts were lower than that of SBA-15 support. Increased metal loadings could lead to higher concentrations of $Ce_{1-x}Zr_xO_2$ compounds that were accommodated in the SBA-15 support's porous channels. This could partially block the pores, reducing their accessibility and effectively reducing their pore volume. Likewise, as the metal loadings increased, there was a higher concentration of Ce and Zr metal ions present on the SBA-15 support's surface. Those compounds tended to agglomerate and form larger clusters, which in turn could partially obstruct the micropores within the SBA-15 support.

In conclusion, the successful synthesis of all $Ce_{1-x}Zr_xO_2$/SBA-15 catalysts was confirmed through the consistent findings of various researchers, whereby similar observations regarding the changes in surface and pore characteristics with increasing metal loadings were reported [13, 30–32]. Nevertheless, it was observed that the SBA-15 support could accommodate metal loadings of up to 40 wt% without causing their total surface area and porosity to experience a significant loss. This was an advantage of this ordered mesoporous SBA-15 support over other non-ordered supports such as C [33–35], $Mg(OH)_2$ [36], and TiO_2 [37]. Thus, the potential drawbacks of pore narrowing and partial pore-blocking at higher active metal loadings could have offset the advantage of having an increased amount of active metal present.

Figure 1a illustrates the N_2 physisorption isotherms, while Fig. 1b represents the BJH pore size distribution profiles of SBA-15 support, $5Ce_{1-x}Zr_xO_2$/SBA-15, $10Ce_{1-x}Zr_xO_2$/SBA-15, $20Ce_{1-x}Zr_xO_2$/SBA-15, $30Ce_{1-x}Zr_xO_2$/SBA-15, and $40Ce_{1-x}Zr_xO_2$/SBA-15 catalysts, respectively. These figures provide a better understanding of their surface characteristics.

As shown in Fig. 1a, similar to SBA-15 support, all synthesized catalysts demonstrated the standard type IV isotherm indicative of mesoporous materials. Thus, this also implied that the SBA-15 support's hexagonal structure remained unchanged even after the impregnation of $Ce_{1-x}Zr_xO_2$ compounds at high loadings up to metal

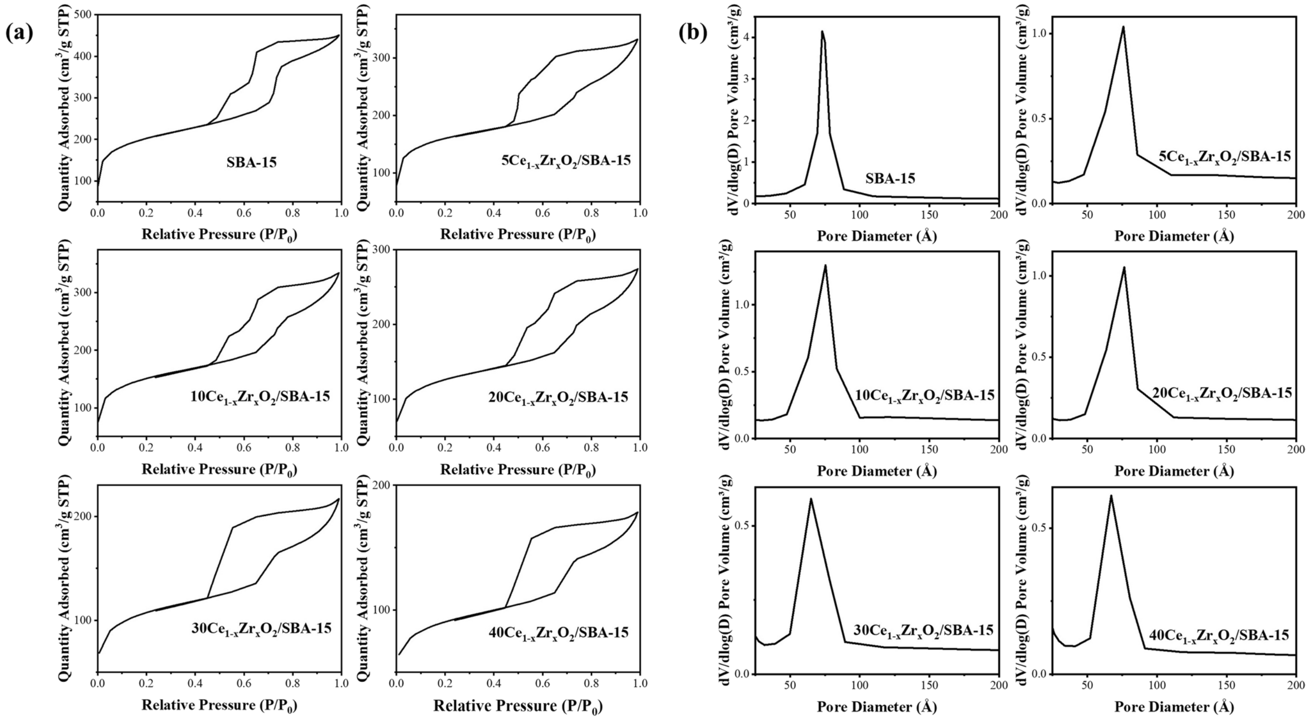

Fig. 1 **a** N_2 physisorption isotherms and **b** BJH pore size distribution profiles of SBA-15 support and $y\mathrm{Ce}_{1-x}\mathrm{Zr}_x\mathrm{O}_2$/SBA-15 catalysts

loading of 40 wt%. Moreover, all isotherms are characterized by typical hysteresis loops of H1-type isotherms with narrow pore size distribution and closures occurring at relative pressures (P/P_0) between 0.45 and 1. Moreover, all isotherms in Fig. 1a indicate two distinct regions; firstly, nitrogen adsorption takes place in a monolayer fashion at a relative pressure below 0.2, and then, after that relative pressure, nitrogen adsorption in a multilayer fashion is started. Similarly, the closure of the hysteresis loop, which falls within the second region, is characterized by typical capillary condensation occurring inside the catalyst's mesopores.

Besides, from the isotherms in Fig. 1a, it could be deduced that all synthesized catalysts at different metal loadings (5–40 wt%) resulted in highly porous materials with uniformly arranged meso-sized pores. Also, it is noteworthy to mention that despite having the same type of isotherms, nitrogen uptake significantly decreased with increasing metal loadings. The decrease in nitrogen uptake could be associated with the reductions in specific surface and pore volume as shown in Table 1, which was caused by pore plugging by denser $\mathrm{Ce}_{1-x}\mathrm{Zr}_x\mathrm{O}_2$ compounds with increasing loadings. Nevertheless, there was a strong resemblance between the shape of the hysteresis curves of the synthesized catalysts and that of the SBA-15 support. In short, this indicated that the synthesis of mesoporous $\mathrm{Ce}_{1-x}\mathrm{Zr}_x\mathrm{O}_2$/SBA-15 catalysts at all five varying metal loadings resulted in uniform pore shapes and distributions.

As shown in Fig. 1b, SBA-15 support had pore size distributions within the range of 50 Å to 100 Å. In the meantime, $5\mathrm{Ce}_{1-x}\mathrm{Zr}_x\mathrm{O}_2$/SBA-15, $10\mathrm{Ce}_{1-x}\mathrm{Zr}_x\mathrm{O}_2$/SBA-15, and $20\mathrm{Ce}_{1-x}\mathrm{Zr}_x\mathrm{O}_2$/SBA-15 catalysts exhibited pore size distributions ranging from 35 to 110 Å, while $30\mathrm{Ce}_{1-x}\mathrm{Zr}_x\mathrm{O}_2$/SBA-15 and $40\mathrm{Ce}_{1-x}\mathrm{Zr}_x\mathrm{O}_2$/SBA-15 catalysts demonstrated pore size distributions ranging from 35 to 100 Å, respectively. Thus, this demonstrates that all the synthesized catalysts exhibited relatively narrow pore size distributions within the meso-size range. A narrow range of pore sizes in the catalysts suggested that the pores were formed with regularity and in an organized manner.

Also, Fig. 1b provides a clear depiction that catalysts with lower metal loadings (5–20 wt%) exhibited wider pore size distributions, while catalysts with higher metal loadings (30–40 wt%) displayed narrower pore size distributions. The observed phenomenon could be associated with the presence of higher concentrations of $\mathrm{Ce}_{1-x}\mathrm{Zr}_x\mathrm{O}_2$ compounds at higher loadings, which likely resulted in partial pore blockage within the SBA-15 support's large mesopores. The findings of this study were in complete agreement with the research paper published by Yan and his research group [38]. The progressive reduction in surface area and pore volume with increasing metal loadings as shown in Table 1 provided additional evidence supporting the above observation.

The broadening of pore size distributions in the $5\mathrm{Ce}_{1-x}\mathrm{Zr}_x\mathrm{O}_2$/SBA-15, $10\mathrm{Ce}_{1-x}\mathrm{Zr}_x\mathrm{O}_2$/SBA-15, and $20\mathrm{Ce}_{1-x}\mathrm{Zr}_x\mathrm{O}_2$/SBA-15 catalysts, on the other hand, could be due to the formation of secondary or interparticle pores. The existence of these secondary or interparticle pores was previously reported by a few researchers in early studies [39, 40]. In summary, the surface and pore characteristics of all synthesized catalysts in various metal loadings indicated that they were successfully synthesized as the typical characteristics of SBA-15 support were maintained even at high $Ce_{1-x}Zr_xO_2$ loadings up to 40 wt%.

Surface Morphology Analysis

Figure 2 illustrates the FESEM micrographs of SBA-15 support and all the synthesized catalysts with different metal loadings. Generally, the FESEM micrographs revealed that SBA-15 support and all the synthesized catalysts of different catalyst loadings displayed the typical morphology of SBA-15, featuring elongated meso-channels and fibrous structures with a uniform size of approximately 0.5 µm [27, 41–43].

While the synthesized catalysts generally maintained the typical morphology of the SBA-15 support, it was evident that $30Ce_{1-x}Zr_xO_2$/SBA-15 and $40Ce_{1-x}Zr_xO_2$/SBA-15 exhibited a more prominent presence of swirling patterns than the other catalysts. Furthermore, significant swirling was observed to cause some of the elongated tubular structures of SBA-15 support to be curved and form round clusters. Still, due to the amorphism of SBA-15 support, the newly formed $Ce_{1-x}Zr_xO_2$ bonds could exhibit arbitrary angles and lengths lacking any consistent pattern or predictable behavior in the modification of SBA-15 support's structure. This observation, however, seemed to align with a statement reported in the study by Bhange et al. [44].

Moreover, Fig. 2 reveals the presence of very minimal deposits or crystals (indicated by small circles) on the external surface of $5Ce_{1-x}Zr_xO_2$/SBA-15 and $10Ce_{1-x}Zr_xO_2$/SBA-15 catalysts. At such low metal loadings, the $Ce_{1-x}Zr_xO_2$ compounds were preferably embedded inside the SBA-15 support's internal mesopores. Also, relatively more deposits or crystals were found on the external surface of the catalysts as the metal loadings increased, as displayed in Fig. 2. In fact, there was a higher tendency for the formation of deposits or metal clusters on the SBA-15 external surfaces at higher metal loadings due to the partial narrowing of the tubular meso-channels. This observation was in great agreement with the findings in Table 1, where the specific surface areas, external surface areas, and pore sizes decreased with increasing metal loadings. In addition, this observation was consistent with previous reports, which indicated that during the initial stages, metal incorporation was more likely to occur within the internal pores, whereas excessive metal loadings led to preferential deposition on the external surface of the support [27, 43, 45, 46]. Nevertheless, in any case, the FESEM micrographs in Fig. 2 suggest that the incorporation of $Ce_{1-x}Zr_xO_2$ compounds into SBA-15 support still retained the typical meso-structure of SBA-15 even at high metal loadings even up to 40 wt%.

Internal Morphology Analysis

To visually examine the changes in the internal morphological structure of SBA-15 support upon impregnation with $Ce_{1-x}Zr_xO_2$ compounds at different metal loadings, TEM analysis was performed. Figure 3 displays TEM micrographs of the SBA-15 support and all synthesized catalysts at varying metal loadings. It could be seen that the micrographs of each sample demonstrated long, well-ordered mesoporous channels of SBA-15. Also, it should be noted that the TEM micrographs revealed that the elongated meso-channels of all synthesized catalysts were curved, like that of the SBA-15 support.

The TEM micrographs obtained in Fig. 3 were also consistent with the findings from previous studies [41, 42]. Hence, this proved that the extremely ordered organization of the pore channels remained intact even after the incorporation of $Ce_{1-x}Zr_xO_2$ compounds up to 40 wt% metal loadings. Besides, these observations further confirmed that the impregnation of $Ce_{1-x}Zr_xO_2$ compounds did not cause any severe changes in the structural features of SBA-15 support since there were no signs of significant internal mesopore deformations shown in all the TEM micrographs in Fig. 3.

Furthermore, in all cases, TEM micrographs did not reveal any notable aggregation of $Ce_{1-x}Zr_xO_2$ species, revealing that the $Ce_{1-x}Zr_xO_2$ compounds were distributed in a nearly homogeneous manner within the SBA-15 support's framework; probably within the mesopores. In short, based on the FESEM micrographs (Fig. 2) and TEM micrographs (Fig. 3), it could be concluded that all synthesized catalysts maintained their original elongated meso-channeled morphology of SBA-15 support, even at high metal loadings up to 40 wt.%.

Elemental Composition Analysis

EDX analysis was performed to determine the presence as well as the nominal elemental composition of O, Si, Ce, and Zr elements in the SBA-15 support, $5Ce_{1-x}Zr_xO_2$/SBA-15, $10Ce_{1-x}Zr_xO_2$/SBA-15, $20Ce_{1-x}Zr_xO_2$/SBA-15, $30Ce_{1-x}Zr_xO_2$/SBA-15, and $40Ce_{1-x}Zr_xO_2$/SBA-15 catalysts, respectively. The surface elemental compositions of all synthesized catalysts are represented in Table 2.

In general, the composition of Si elements in all synthesized catalysts was almost similar to that of SBA-15 support. This implied that the surface characteristics of SBA-15 remained unchanged even after the incorporation of $Ce_{1-x}Zr_xO_2$ compounds at different metal loadings. An intriguing trend was observed regarding the compositions of Ce and Zr elements, which showed an increase

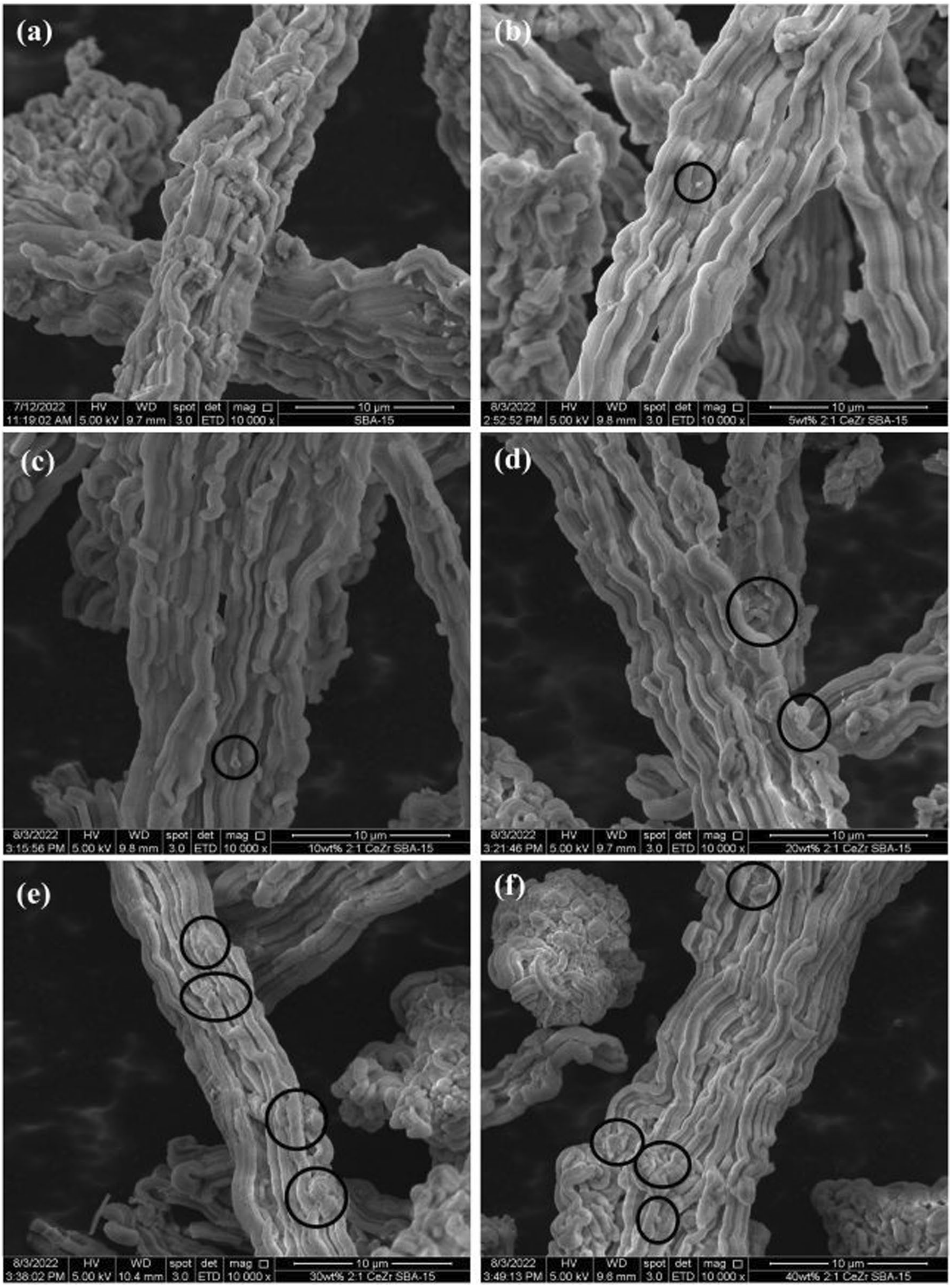

Fig. 2 FESEM micrographs of **a** SBA-15 support, **b** 5$Ce_{1-x}Zr_xO_2$/SBA-15, **c** 10$Ce_{1-x}Zr_xO_2$/SBA-15, **d** 20$Ce_{1-x}Zr_xO_2$/SBA-15, **e** 30$Ce_{1-x}Zr_xO_2$/SBA-15, and **f** 40$Ce_{1-x}Zr_xO_2$/SBA-15 catalysts at a magnification of 10000×

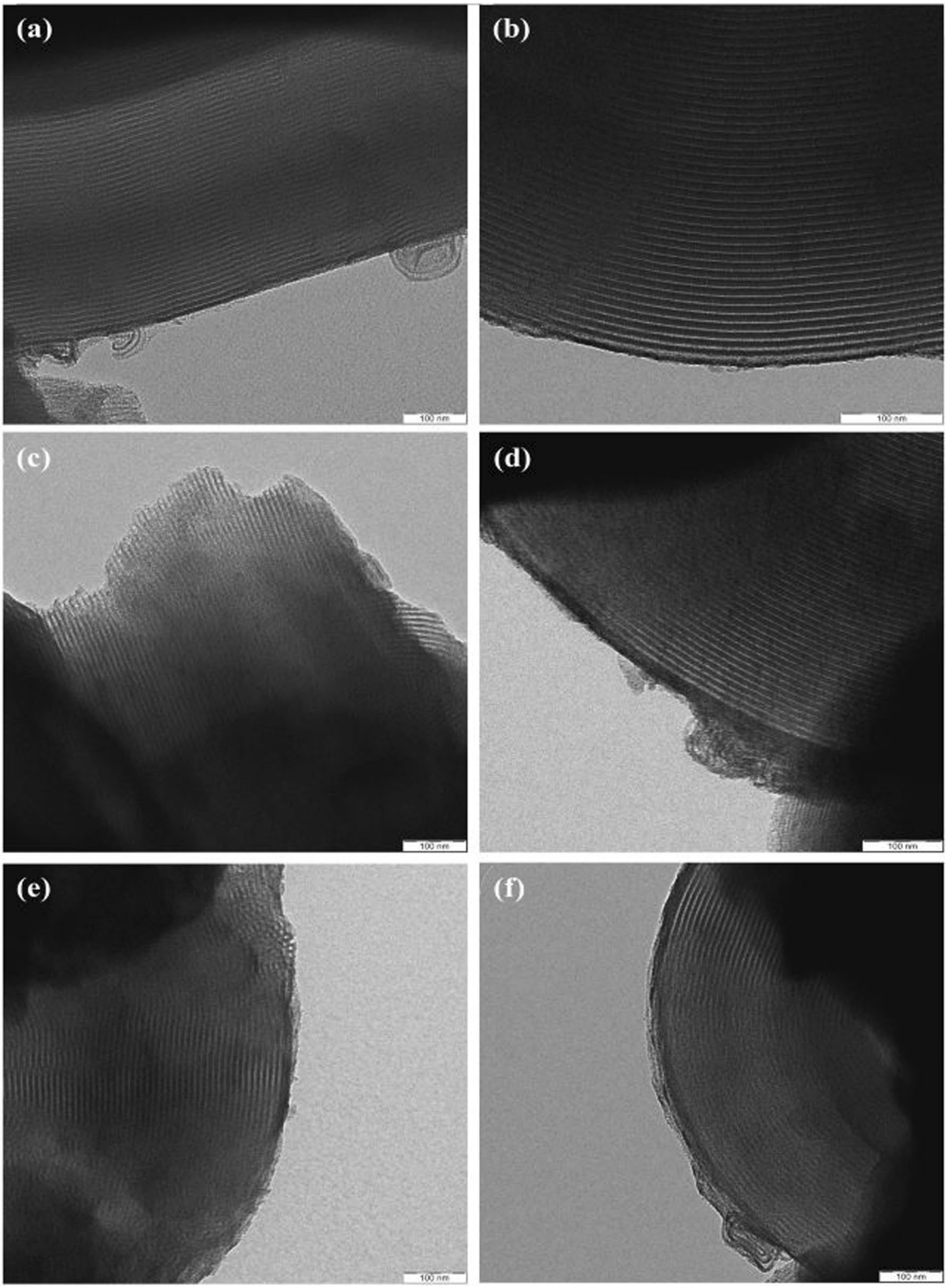

Fig. 3 TEM micrographs of **a** SBA-15 support, **b** 5$Ce_{1-x}Zr_xO_2$/SBA-15, **c** 10$Ce_{1-x}Zr_xO_2$/SBA-15, **d** 20$Ce_{1-x}Zr_xO_2$/SBA-15, **e** 30$Ce_{1-x}Zr_xO_2$/SBA-15, and **f** 40$Ce_{1-x}Zr_xO_2$/SBA-15 catalysts at a magnification of 40000×

Table 2 Elemental composition of SBA-15 support, $y\mathrm{Ce}_{1-x}\mathrm{Zr}_x\mathrm{O}_2$/SBA-15, and spent $10\mathrm{Ce}_{1-x}\mathrm{Zr}_x\mathrm{O}_2$/SBA-15 catalysts

Catalyst	Elemental composition (wt%)			
	O	Si	Ce	Zr
SBA-15	76.61	23.39	0	0
$5\mathrm{Ce}_{1\text{-}x}\mathrm{Zr}_x\mathrm{O}_2$/SBA-15	70.66	23.32	6.02	0
$10\mathrm{Ce}_{1\text{-}x}\mathrm{Zr}_x\mathrm{O}_2$/SBA-15	71.32	20.32	7.42	0.94
$20\mathrm{Ce}_{1\text{-}x}\mathrm{Zr}_x\mathrm{O}_2$/SBA-15	64.5	24.66	9.44	1.4
$30\mathrm{Ce}_{1\text{-}x}\mathrm{Zr}_x\mathrm{O}_2$/SBA-15	68.36	20.11	9.95	1.58
$40\mathrm{Ce}_{1\text{-}x}\mathrm{Zr}_x\mathrm{O}_2$/SBA-15	66.49	21.91	9.56	2.04
R1	72.33	20.36	6.53	0.78
R2	73.48	20.11	6.13	0.28
R3	73.87	19.62	5.4	1.11
R4	73.23	19.89	5.54	1.34

with increasing metal loadings from 5 to 40 wt% catalysts. Except for the $40\mathrm{Ce}_{1-x}\mathrm{Zr}_x\mathrm{O}_2$/SBA-15 catalyst, where the composition of the Ce element was slightly lower than the $30\mathrm{Ce}_{1-x}\mathrm{Zr}_x\mathrm{O}_2$/SBA-15 catalyst, this deviation remained negligible. This discrepancy may be attributed to agglomeration observed at higher catalyst loadings, specifically at 40 wt%, which could be evident at a specific region on the external surface and potentially remain unaccounted for during EDX measurements, leading to a lower recorded composition of Ce element in $40\mathrm{Ce}_{1-x}\mathrm{Zr}_x\mathrm{O}_2$/SBA-15 catalyst than that of the $30\mathrm{Ce}_{1-x}\mathrm{Zr}_x\mathrm{O}_2$/SBA-15 catalyst.

Based on the elemental composition data tabulated in Table 2, it could be concluded that the recorded elemental compositions of the synthesized catalysts were qualitatively consistent with the metal loadings of the prepared catalysts, hence, evidently indicating the effectiveness of the preparation method. It should, however, be noted that there were discrepancies in the element concentrations given in Table 2 compared to actual concentrations. This is because EDX analysis was performed only externally to the surface of the catalysts. Thus, the entrapped elements in the internal mesopores might be undetected and taken into account in this analysis.

Functional Group and Chemical Bond Analysis

FTIR analysis was done to evaluate the formation and interaction of $\mathrm{Ce}_{1-x}\mathrm{Zr}_x\mathrm{O}_2$ compounds in all SBA-15-supported catalysts at varying metal loadings. Figure 4 depicts the FTIR spectra (400–4000 cm^{-1}) of $5\mathrm{Ce}_{1-x}\mathrm{Zr}_x\mathrm{O}_2$/SBA-15, $10\mathrm{Ce}_{1-x}\mathrm{Zr}_x\mathrm{O}_2$/SBA-15, $20\mathrm{Ce}_{1-x}\mathrm{Zr}_x\mathrm{O}_2$/SBA-15, $30\mathrm{Ce}_{1-x}\mathrm{Zr}_x\mathrm{O}_2$/SBA-15, and $40\mathrm{Ce}_{1-x}\mathrm{Zr}_x\mathrm{O}_2$/SBA-15 catalysts.

As indicated in the figure, the broad Si–O–Si band, from 1220 to 1076 cm^{-1} originating from the asymmetric stretching of Si–O–Si, which was commonly found in the condensed silica network of SBA-15, was found in SBA-15 support and all synthesized catalysts. Furthermore, SBA-15 support and all synthesized catalysts from 5 to 40 wt% also exhibited the symmetric stretching of Si–O–Si at 800 cm^{-1}, and the bending vibration of Si–O–Si at 451 cm^{-1} [43]. As seen in Fig. 4, an observable peak at 962 cm^{-1} was attributed to the vibrational mode of defective Si–OH bonds formed during the functionalization of TEOS during the SBA-15 support synthesis. These bands, present in both SBA-15 support and all synthesized catalysts at varying loadings, suggested that the silica network was formed successfully. The mesoporous structure remained unchanged even when $\mathrm{Ce}_{1-x}\mathrm{Zr}_x\mathrm{O}_2$ compounds were impregnated into the SBA-15 support. One of the most interesting discoveries was the figure showed a strong absorption peak at 3440 cm^{-1}. This occurrence was ascribed to the stretching vibration of -OH groups in lattice water attached between Si–OH from the SBA-15 support and water molecules or other polar components at the $\mathrm{Ce}_{1-x}\mathrm{Zr}_x\mathrm{O}_2$ compounds' surface. Also, the presence of other polar components forming H bonds with the Si–OH molecules could also cause the appearance of this band [43, 47, 48].

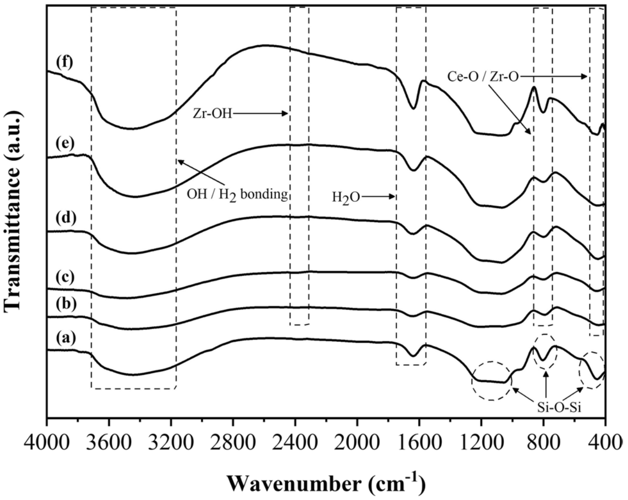

Fig. 4 FTIR spectra of **a** SBA-15 support, **b** $5\mathrm{Ce}_{1-x}\mathrm{Zr}_x\mathrm{O}_2$/SBA-15, **c** $10\mathrm{Ce}_{1-x}\mathrm{Zr}_x\mathrm{O}_2$/SBA-15, **d** $20\mathrm{Ce}_{1-x}\mathrm{Zr}_x\mathrm{O}_2$/SBA-15, **e** $30\mathrm{Ce}_{1-x}\mathrm{Zr}_x\mathrm{O}_2$/SBA-15, and **f** $40\mathrm{Ce}_{1-x}\mathrm{Zr}_x\mathrm{O}_2$/SBA-15 catalysts

Moreover, a band at 1630 cm^{-1}, which signified the presence of bending vibration of -OH groups of adsorbed molecules, was present in all the synthesized catalysts, including the SBA-15 support. The rapid adsorption of water molecules into the mesopores of SBA-15 support can be explained by the existence of hydrophilic Si–OH groups in the support material [41] as well as the surrounding air humidity [49].

As indicated in the FTIR spectra, all synthesized catalysts had a strong absorption band in the range of 3100 cm^{-1} to 3700 cm^{-1} due to stretching vibration of externally adsorbed

-OH groups of water molecules on the $Ce_{1-x}Zr_xO_2$ compounds of the catalysts [50, 51]. Also, all synthesized catalysts demonstrated a peak centered at 1630 cm^{-1} indicating the bending vibrational mode of -OH groups of water molecules similar to the SBA-15 support in Fig. 4a. Furthermore, all catalysts exhibited a weak hump at 2390 cm^{-1} indicating the presence of stretching vibration of the Zr–OH bond. However, the peak was nearly absent in the $40Ce_{1-x}Zr_xO_2$/SBA-15 catalyst.

Furthermore, the FTIR spectra of all synthesized catalysts revealed distinct characteristics, with strong symmetric stretching vibrations of Ce–O and Zr–O bonds at 540 cm^{-1} and weak symmetric stretching vibrations of Ce–O and Zr–O bonds at 825 cm^{-1}, indicating the presence of $Ce_{1-x}Zr_xO_2$ compounds in the catalysts. Also, it should be noted that the intensities of the peaks at 540 cm^{-1} and 825 cm^{-1} exhibited an increase as metal loadings increased. This suggested the existence of a higher $Ce_{1-x}Zr_xO_2$ compound concentration in the catalysts at higher loadings. Therefore, the successful incorporation of $Ce_{1-x}Zr_xO_2$ compounds into SBA-15 support was achieved in all synthesized catalysts from metal loadings of 5 wt% up to 40 wt%.

However, overlapping between two peaks in the FTIR spectra can result in the absence of certain peaks, as the combined peaks obscure the individual contributions. In this way, a peak at about 460 cm^{-1}, signifying the stretching vibration of Ce–O and Zr–O of the CeO_2 and ZrO_2 phases, respectively [50, 51], was masked by the Si–O–Si bending vibration peak. The same occurrence was also observed for a peak at about 825 cm^{-1}, which was typical for any metal–O stretching vibration [52], and was indistinguishable in the spectra due to overlapping with the Si–O–Si symmetric stretching band. In general, the typical bands of SBA-15 support were also found in all the synthesized catalysts, even at different metal loadings, indicating the successful formation of the silica network. Despite the impregnation of $Ce_{1-x}Zr_xO_2$ compounds even at high loadings up to 40 wt%, the mesoporous structure remained unaffected.

Catalytic Activity Test

Influence of Metal Loading

This section was focused on investigating the influence of metal loading on glycerol conversion and lactic acid yield. $Ce_{1-x}Zr_xO_2$/SBA-15 catalysts with varying total metal loadings (5 wt%, 10 wt%, 20 wt%, 30 wt%, and 40 wt%) on SBA-15 support were employed for catalyzing the reaction, whilst other parameters such as catalyst-to-glycerol loading, reaction temperature, and reaction time were kept constant at 20 wt%, 250 °C, and 2 h, respectively. The catalytic performance of all synthesized catalysts in terms of glycerol conversion and lactic acid yield is depicted in Fig. 5.

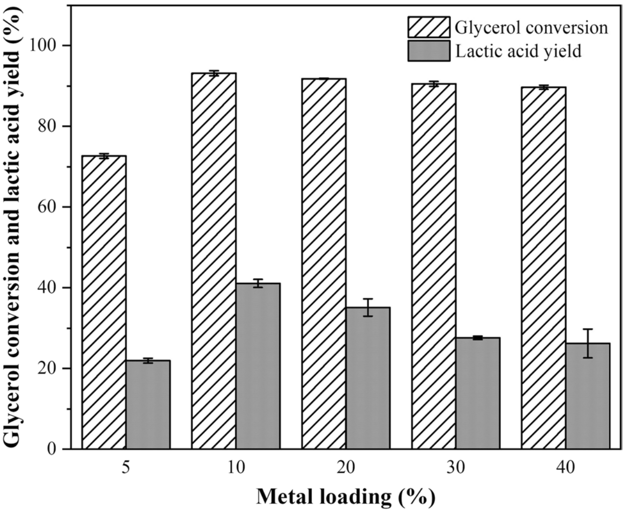

Fig. 5 Performance of $5Ce_{1-x}Zr_xO_2$/SBA-15, $10Ce_{1-x}Zr_xO_2$/SBA-15, $20Ce_{1-x}Zr_xO_2$/SBA-15, $30Ce_{1-x}Zr_xO_2$/SBA-15, and $40Ce_{1-x}Zr_xO_2$/SBA-15 catalysts on selective glycerol-to-lactic acid oxidation

In general, Fig. 5 demonstrates remarkable glycerol conversions, ranging from 72.7% to 93.2%, achieved consistently for all catalysts in different metal loadings (5–40 wt%). The glycerol conversion exhibited an upward trend, increasing from 72.7% to 93.2% when the metal loading increased from 5 to 10 wt%. However, a gradual decrease in conversion was observed thereafter, reaching 89.7% at a metal loading of 40 wt%. Interestingly, a similar pattern to glycerol conversion was also observed in lactic acid yield. The catalytic performance, especially the lactic acid yield obtained in this work was noteworthy, particularly when considering that an initial glycerol concentration more than 13 folds higher (13.23 M) was used compared to the work by Yin et al. [25], where approximately 90% glycerol conversion was achieved using a NiO/graphite catalyst.

The $10Ce_{1-x}Zr_xO_2$/SBA-15 catalyst demonstrated the highest catalytic performance, with a glycerol conversion and a lactic acid yield of 93.2% and 41.1%, respectively, while the lowest catalytic performance with a lactic acid yield as low as 22% was exhibited by the $5Ce_{1-x}Zr_xO_2$/SBA-15 catalyst. However, it was worth mentioning that the decrease in glycerol conversion at increasing metal loadings from 20 to 40 wt% catalysts was very marginal, while the decrease in lactic acid yield was substantial. The reduction in lactic acid yield, as metal loadings increased, could be associated with enhanced catalytic capability for over-oxidation reactions and/or C–C bond cleavage to acetic acid, glyceric acid, glycolic acid, pyruvic acid, and oxalic acid.

The lowest catalytic activity of the $5Ce_{1-x}Zr_xO_2$/SBA-15 catalyst was simply due to the catalyst's lowest active metal content. The presence of only 5 wt% of metal sites proved to be insufficient for effective reaction occurrence, thus indicating a reaction-controlling system. Simultaneously, this result also indicated the rapid internal diffusion of the reactant within the SBA-15 support's mesoporous channels [53]. Regardless of the 5$Ce_{1-x}Zr_xO_2$/SBA-15 catalyst, the highest total surface area, total pore volume, and average pore size was exhibited by the 10$Ce_{1-x}Zr_xO_2$/SBA-15 catalyst, as presented in Table 1. Hence, it could be inferred that the 10$Ce_{1-x}Zr_xO_2$/SBA-15 catalyst had a sufficiently high dispersion of active metals and an additional amount of metal sites were readily accessible by the glycerol molecules. Nevertheless, the marginal reduction in glycerol conversion with increasing the metal loadings from 10 to 40 wt% demonstrated that higher active metal loadings did not guarantee enhanced accessibility for glycerol molecules. The presence of larger and more metal deposits or crystals on the SBA-15 support's external surface, as depicted in the FESEM micrographs in Fig. 2, further supports this claim.

Moreover, the utilization of the 10$Ce_{1-x}Zr_xO_2$/SBA-15 catalyst produced glycerol conversion and lactic acid yield comparable to those reported in earlier research [30, 54]. In contrast, although a high lactic acid yield of 97% was achieved using the Cu5CaMg catalyst as reported by Bruno et al. [55], the actual concentration of lactic acid obtained in their study was relatively low due to the low initial glycerol concentration of only 20 vol.% used. Thus, the active components played a positive role in lactic acid production, and when combined with the shape-selective effect of the mesoporous SBA-15 support, nearly half of the resulting products consisted of the desired product. As depicted in Fig. 5, a substantial decrease in lactic acid yield was noted for metal loadings above 10 wt%, despite almost consistent glycerol conversions. These findings indicated that the shape selectivity effect was most pronounced in the 10$Ce_{1-x}Zr_xO_2$/SBA-15 catalyst, surpassing the other catalysts.

This observation was consistent with the catalysts' surface properties in Table 1, wherein the 10$Ce_{1-x}Zr_xO_2$/SBA-15 catalyst exhibited comparatively high total surface area and average pore size. The significant internal mesopore area of the catalyst facilitated glycerol molecules' accessibility to the active metal sites. This, in turn, enhanced the catalytic reaction, particularly in the initial step of glycerol-to-lactic acid transformation, which typically involves glycerol-to-glyceraldehyde dehydrogenation. The primary occurrence of this process takes place at the catalyst's metallic sites. However, as the active metal loadings increased, the narrowing of the internal pores might cause the reaction site to gradually be shifted from the internal mesopores to the external surface with larger pores. Therefore, the shape-selective effect diminished, resulting in a decline in the yield of lactic acid.

Furthermore, the 10$Ce_{1-x}Zr_xO_2$/SBA-15 catalyst exhibited an average pore size of 51.33 Å (Table 1), which also hindered the formation of by-products such as 2-hydroxypropenal [56]. This finding aligns with previous findings which demonstrated that catalysts with average pore sizes of around 50 Å or smaller typically exhibited comparatively lower selectivity towards lactic acid, in contrast to catalysts with larger pore diameters [57]. This observation confirms that the mesoporous 10$Ce_{1-x}Zr_xO_2$/SBA-15 catalyst used had favorable pore characteristics for shape selectivity to facilitate lactic acid formation from glycerol. Specifically, this could be attributed due to the shape selectivity effect observed during the intramolecular Cannizzaro reaction of pyruvaldehyde to lactic acid [18]. Hence, the increased surface area and average pore size, allowed for improved adsorption and interaction of reactant molecules, leading to increased effective collisions and ultimately resulting in a greater lactic acid yield. Similar findings were also reported by several studies [25, 35, 54, 58]. Hence, it could be concluded that the best metal loading was 10 wt%, ensuring an even distribution of both metals in the SBA-15 mesopores.

Influence of Catalyst Loading

In this section, the influence of catalyst loadings on catalytic performance was explored. The loadings of the 10$Ce_{1-x}Zr_xO_2$/SBA-15 catalyst within the range of 5 wt% to 40 wt% were varied relative to the amount of glycerol whilst keeping the reaction temperature and reaction time constant at 250 °C and 2 h, respectively. Figure 6 presents the results of glycerol conversion and lactic acid yield using the 10$Ce_{1-x}Zr_xO_2$/SBA-15 catalyst at different catalyst loadings.

As shown in Fig. 6, initially increasing the catalyst loading from 5 to 25 wt% resulted in a progressive enhancement in glycerol conversion. However, at 30 wt% loading a slight decrease was observed in the glycerol conversion,

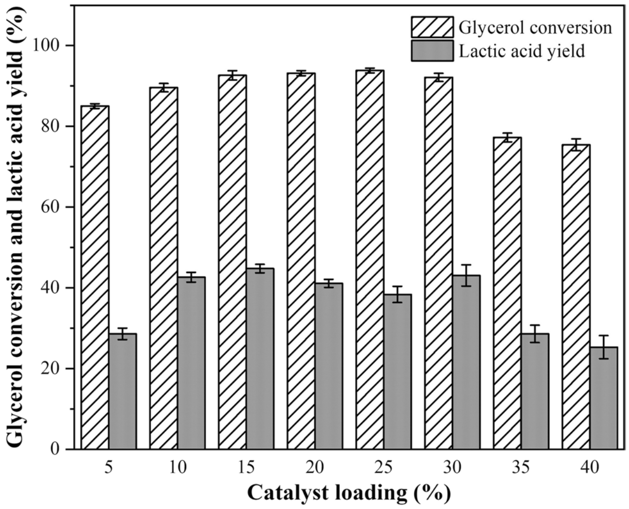

Fig. 6 Performance of 10$Ce_{1-x}Zr_xO_2$/SBA-15 catalyst on selective glycerol-to-lactic acid oxidation at different catalyst loadings relative to the amount of glycerol

reaching a value of 92.1%. Surprisingly, a significant drop in glycerol conversion occurred when the catalyst loading was increased further to 35 wt%, plummeting from 92.1% to 77.2%. The decline in glycerol conversion continued to 75.4% at 40 wt% loading. Also, it should be noted that between catalyst loadings of 15 wt% and 30 wt%, the variations in glycerol conversion were very marginal, indicating relatively stable performance within this range. Such observations could potentially be attributed to the equilibrium established between the intermediates and/or by-products during the reaction [57, 59].

Furthermore, it was worth mentioning that a 44.8% lactic acid yield, which was the highest recorded yield so far, was achieved at a catalyst loading of 15 wt%. Interestingly, any subsequent increase in catalyst loading proved to be detrimental except for 30 wt% loading as shown in Fig. 6. In general, these findings suggested a substantial decrease in the lactic acid selectivity occurred during the reaction and was accompanied by the generation of an increased formation of intermediates and/or by-products instead of lactic acid. The reason for this was mainly because there was an increased concentration of active sites available for glycerol dehydrogenation, which was followed by the hydration of aldehyde intermediates, including glyceraldehyde and pyruvaldehyde, within the reaction system.

In addition, the influence of equilibrium limitations was expected to be more pronounced at higher catalyst loadings, primarily due to the greater extent of the reaction resulting in the accumulation of a higher number of intermediates within the reaction system. Consequently, competing reactions became more significant, causing rapid depletion of these intermediates and leading to the formation of by-products (e.g., pyruvic acid, glyceric acid, and lactaldehyde) other than lactic acid. It was possibly because as the catalyst loading increased, the catalyst particles began to agglomerate, leading to reduced accessibility of the glycerol and intermediates to the catalyst. Therefore, the active sites externally attached to the surface of these agglomerates became actively involved in the reaction, hindering the internal mass transfer rates to the active sites within the aggregates [60].

Interestingly, several researchers reported similar trends in lactic acid yield while manipulating the catalyst loading relative to the amount of glycerol [30, 45, 54, 61]. Beyond a certain catalyst loading, further increases failed to yield the desired effect, instead, a significant drop in the lactic acid yield was observed. Thus, it might not be advantageous to use more catalysts at high conversions, as the reaction was governed by equilibrium. In conclusion, the best catalytic performance was achieved using a 10$Ce_{1-x}Zr_xO_2$/SBA-15 catalyst with a lactic acid yield as high as 44.8%, at a glycerol conversion of 92.6% with 15 wt.% catalyst loading, as far as achieving the maximum yield of lactic acid was in concern.

Influence of Reaction Temperature

The influence of reaction temperature on the catalytic performance of 10CeZr/SBA-15 was studied. The study involved varying the reaction temperature between 240 and 270 °C. Lower temperatures were excluded from the study due to the observed poor catalytic activity at those temperatures. On the other hand, higher temperatures were avoided because they led to the production of unpleasant-smelling compounds, indicating a significant decomposition of the reaction products. Figure 7 depicts the glycerol conversions and lactic acid yields of 10$Ce_{1-x}Zr_xO_2$/SBA-15 catalyst at different reaction temperatures over a 3 h reaction.

Raising the temperature can lead to enhanced interaction between reactants and catalysts, a decrease in viscosity, and improved solubility. Moreover, it has the potential to enhance the diffusion of reactants, intermediates, and products within the active sites, facilitating their movement in and out [62]. In Fig. 7a, at a reaction temperature of 240 °C, glycerol conversion steadily increased from 20.2% at 0.5 h to 63.2% at 1.5 h. Subsequently, at 2 h, there was a sharp and abrupt increment in the glycerol conversion, reaching 91.3%, and it remained consistently high, averaging 91.1% thereafter. Similarly, the lactic acid yield profile exhibited a continuous increase, rising from 3.6% to 25.8% as the reaction time increased. At a reaction temperature of 250 °C (Fig. 7b), glycerol conversion steadily rose from 23.9% to 94.2% over time. Meanwhile, the lactic acid yield profile demonstrated an increase from 10.1% at 0.5 h to 31.7% at 2.5 h, followed by a slight decrease to 29.8% beyond the 2.5 h of reaction.

In addition, Fig. 7c clearly illustrates that at a reaction temperature of 260 °C, the 10$Ce_{1-x}Zr_xO_2$/SBA-15 catalyst consistently maintained a high glycerol conversion rate of 82.9%, even at 0.5 h of reaction time. The glycerol conversion peaked at 94.2% after 2 h of reaction and then gradually declined to 89.1% thereafter. While the conversion increased to 94.21% over time, the yield initially rose from 17.1% to 45.3% after 2 h and subsequently experienced a slight decrease to 32.4% after 3 h of reaction. Similar to the performance at 260 °C (Fig. 7c), the 10$Ce_{1-x}Zr_xO_2$/SBA-15 catalyst exhibited high glycerol conversion right from the start of the reaction at 270 °C (Fig. 7d). The glycerol conversion reached its peak at the 2-h reaction and then experienced a slight decline to 84.9% at the end of the 3 h reaction. Meanwhile, the lactic acid yield increased to a maximum of 37.7% after 2 h of reaction but gradually declined to 30.6% after 3 h.

Based on the conversion profiles presented in Fig. 7, it is evident that the 10$Ce_{1-x}Zr_xO_2$/SBA-15 catalyst consistently demonstrated excellent glycerol conversions, surpassing 90% within just 1.5 h of reaction at both 240 °C and 250 °C. Furthermore, at higher reaction temperatures of 260 °C and

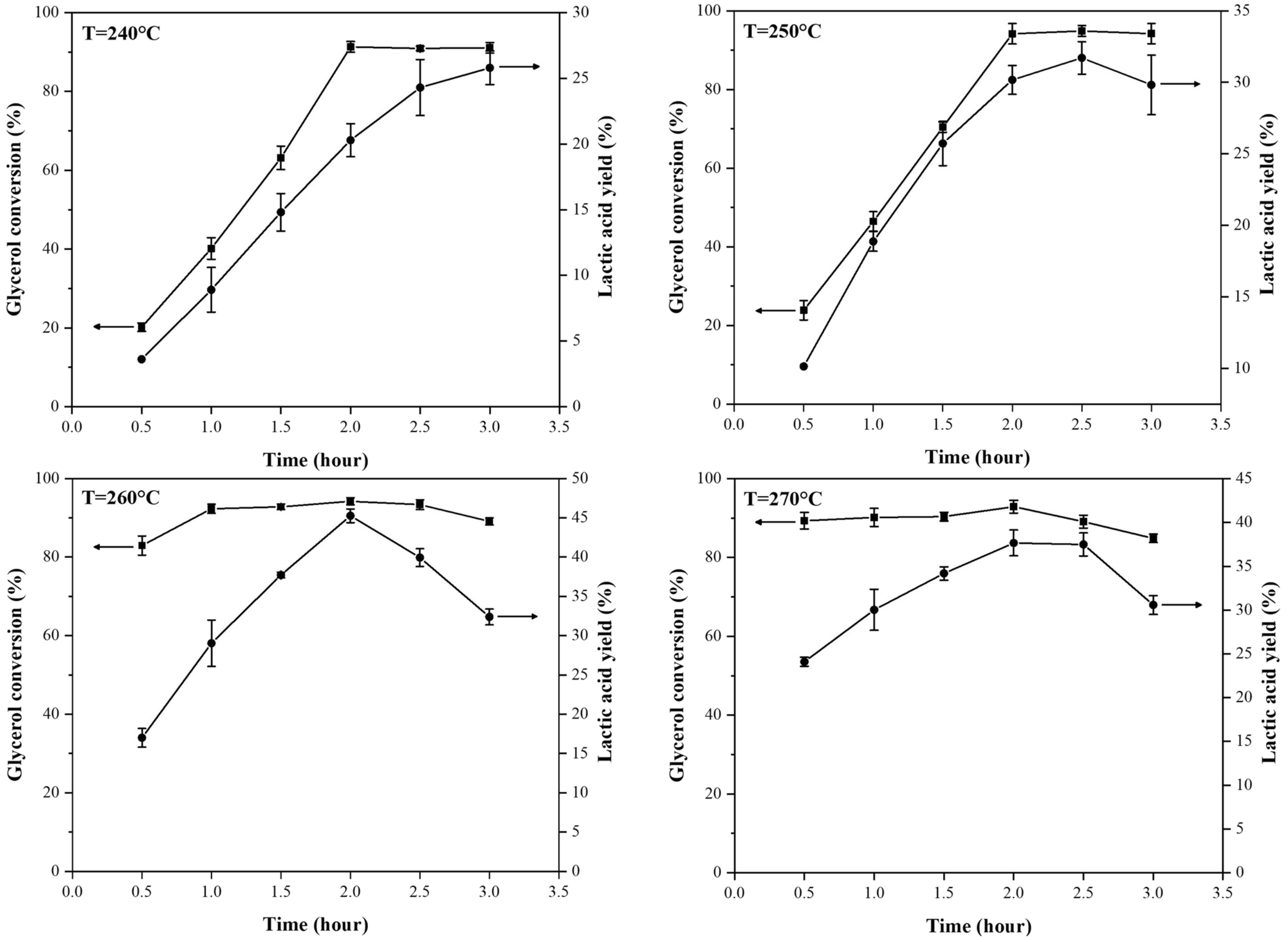

Fig. 7 Performance of $10Ce_{1-x}Zr_xO_2$/SBA-15 catalyst on selective glycerol-to-lactic acid oxidation at different reaction temperatures

270 °C, the glycerol conversion exceeded 90% even within the first hour of the reaction. These findings were consistent with the findings by Bruno et al. [55], wherein in that work, the lowest reaction temperature (200 °C) recorded a glycerol conversion of 72% while increasing the reaction temperature from 220 to 260 °C resulted in glycerol conversions exceeding 90%. As a result, it could be deduced that at higher temperatures, the initial step of the reaction, glycerol-to-glyceraldehyde dehydrogenation via hydrogen abstraction of the glycerol molecule's primary hydroxyl group, was accelerated. This acceleration caused glycerol to rapidly diminish, as evidenced by the high glycerol conversions.

Nevertheless, when the reaction was extended to 2 h, it was notable that the glycerol conversion at a reaction temperature of 270 °C was lower than that observed at 260 °C. This behavior could be attributed to the dehydrogenation reaction's reversible nature, wherein at high concentrations of intermediates (glyceraldehyde and pyruvaldehyde), the reverse reaction could be remarkably enhanced [30]. Thus, it could be inferred that the accelerated production of aldehyde intermediates at a very high temperature (270 °C) through the dehydrogenation reaction was not subsequently supported by a sufficiently fast hydration reaction to form lactic acid. As a result, these accumulated aldehyde intermediates triggered the reverse reaction, leading to the regeneration of glycerol, especially when the reaction time was extended over a longer period, particularly beyond 2 h as indicated by the conversion profiles in Fig. 7. However, it was imperative to note that the decrease in glycerol conversion was very minimal, hence, the reaction could be considered to be leveled off after 2 h.

Furthermore, it could be seen from Fig. 7 that the lactic acid yield remarkably increased from 29.6% to 45.3% with the increase in the reaction temperature from 240 to 260 °C at 2 h of reaction. Upon further increasing the reaction temperature to 270 °C, a noticeable decrease in the lactic acid yield was observed, dropping to 41.8%. Interestingly, while the glycerol conversion remained almost stable beyond 2 h of reaction, the decrease in lactic acid yield indicated a notable increase in secondary reactions which facilitated the generation of additional undesired by-products instead of the desired product, lactic acid. Likewise, similar findings were reported, suggesting that within the first hour of reaction, lactic acid was predominantly generated, after 2–3 h, reaching its optimal concentration and further prolonging the reaction, a gradual decline in lactic acid concentration along with the increase in pyruvic acid were observed [25, 63]. This phenomenon was likely caused by the increased reactivity exhibited by the alkenyl aldehydes (α,β-unsaturated aldehydes) generated during the dehydration reaction. The presence of electron-rich nucleophilic sites in the lactic acid molecule itself is capable of easily participating in a variety of reactions, particularly those that occur at elevated temperatures. These findings were consistent with the work reported by Ramírez-López et al. [9], which reported that elevated temperatures could intensify the thermal decomposition of lactic acid and its intermediate compounds. Along with glyceric acid, acetic acid, pyruvic acid, and other acidic by-products, previous reports had indicated that elevated temperatures, particularly with the aid of highly basic catalysts, could also lead to the formation of additional by-products such as formate and acetate [64–66].

In short, according to Fig. 7, the highest achievable yield of lactic acid was approximately 45.3% with a glycerol conversion of 94.21% after a 2-h reaction conducted at a temperature of 260 °C. At 260 °C, the $10Ce_{1-x}Zr_xO_2$/SBA-15 catalyst demonstrated catalytic performance that was comparable to or even superior to earlier studies. Yin and his co-workers [25] achieved an impressive lactic acid yield, reaching 80.4% at complete glycerol conversion, but they employed a 1 M initial glycerol concentration, which was much lower than that used in this work. In previous investigations conducted by Abdullah et al. [30] and Embong et al. [54], lactic acid yields of 33.7% and 47% were achieved, respectively, with above 90% glycerol conversions but at a reaction temperature as high as 290 °C. The temperature was significantly higher than the temperature range employed in this study, where similar performance was attained. Thus, precise control of the reaction was crucial in facilitating the predominant occurrence of the desired reaction pathway, resulting in the selective formation of lactic acid. In short, 260 °C was the most favorable reaction temperature to generate a lactic acid yield as high as 45.3%, at a 94.2% conversion of glycerol over the $10Ce_{1-x}Zr_xO_2$/SBA-15 catalyst at a 2-h reaction period.

Reusability of the Catalyst

Table 3 Performance of $10Ce_{1-x}Zr_xO_2$/SBA-15 catalyst on selective glycerol-to-lactic acid oxidation for each subsequent reaction cycle

Catalytic run	Catalyst	Conversion (%)	Yield (%)
1	Fresh	94.2	45.3
2	R1	88.6	32.9
3	R2	84.9	38.3
4	R3	78.3	28.6
5	R4	60.3	19.5

The catalytic recycling performance of the $10Ce_{1-x}Zr_xO_2$/SBA-15 catalyst in each cycle of the reaction is presented in Table 3. In general, the $10Ce_{1-x}Zr_xO_2$/SBA-15 catalyst showed good catalytic activity up to three cycles of reaction, with only a slight decrease in catalytic performance after each cycle of reaction. Even after three reaction cycles, the $10Ce_{1-x}Zr_xO_2$/SBA-15 catalyst demonstrated a glycerol conversion of 84.9% and a lactic acid yield of 38.3%. This remarkable performance of the catalyst demonstrated effectiveness and stability throughout multiple cycles of reaction without severe loss of catalytic activity and selectivity for lactic acid.

After four consecutive cycles of reaction, lactic acid yield noticeably decreased from 38.3% to 29.6% accompanied by decreasing glycerol conversion from 84.9% to 78.3%. It could be seen that at the fifth cycle of the reaction, both glycerol conversion and yield of lactic acid continued to decrease further to 60.3% and 19.5%, respectively. In brief, the conversion of glycerol and yield of lactic acid decreased by 33.9% and 25.8% after five cycles of reaction compared to the fresh catalyst, respectively. Moreover, a correlation between the diminishing catalytic activity after each consecutive reaction cycle, as evidenced by the elemental composition analysis results in Table 2 and the increasing average pore sizes presented in Table 1 could be established. Specifically, the composition of Ce and Zr elements exhibited a consistent decrease after each reaction cycle up to the recovered R3 catalyst and the average pore sizes increased up to the recovered catalyst R3. The decrease in Ce and Zr elements composition could result in a depletion of surface-active oxygen species, which were responsible for facilitating the reaction. Meanwhile, increased average pore sizes could facilitate the diffusion of intermediate molecules within the catalyst, which in turn, led to reduced selectivity for lactic acid and potentially favored undesired side reactions. Also, it appeared that during the fourth and fifth cycles of reaction, a significant decline in catalytic activity was observed due to the accumulation and growth of $Ce_{1-x}Zr_xO_2$ compounds externally attached to the surface of SBA-15 support. The formation of agglomerated particles, likely resulting from catalyst sintering, hindered the reactant molecules' accessibility to the active sites, thereby causing a loss in catalytic activity.

In short, the results in Table 3 revealed that the $10Ce_{1-x}Zr_xO_2$/SBA-15 catalyst was reliably reusable up to three cycles of reaction with no appreciable loss in its catalytic activity with a conversion of glycerol and a yield of lactic acid of 84.9% and 38.3%, respectively. Nevertheless, the $10Ce_{1-x}Zr_xO_2$/SBA-15 catalyst demonstrated at least comparable or even superior reusability in this particular reaction compared to previously reported studies using different types of catalysts such as Au/CeO_2, AlPMo, CrPMo, and CuO/ZrO_2 catalysts [21, 48, 57]. This was because exceptionally low initial glycerol concentrations were employed in those reactions compared to this work.

Process Modeling and Kinetic Study

Process Model Development

The $10Ce_{1-x}Zr_xO_2$/SBA-15 catalyst, which demonstrated the highest catalytic performance in selective glycerol-to-lactic acid oxidation was chosen as the model catalyst for process model development and kinetic study investigations. Two separate process models were developed, one specifically for glycerol conversion and the other one specifically for lactic acid yield. After many regressions, the results showed that the glycerol conversion rate could be modeled empirically by using a second-order polynomial equation as a function of reaction temperature and could be expressed as follows:

$$\frac{dx}{dt} = p_1x^2 + p_2x + p_3 \tag{10}$$

where $p_1 = (-0.000575)T^2 + 0.19T - 9.792$, $p_2 = (-0.0019)T^2 + 0.9719T - 122.1$, $p_3 = (-0.001688)T^2 - 0.759T + 85.31$.

Similarly, the rate of lactic acid production as a function of temperature was also modelled and the rate expression was expressed as follows:

$$\frac{dy}{dx} = p_1y^2 + p_2y + p_3 \tag{11}$$

where $p_1 = (0.001198)T^2 - 0.3554T + 10.92$, $p_2 = (-0.003036)T^2 + 1.405T - 161$, $p_3 = (0.0005586)T^2 - 0.2601T + 30.3$.

The models developed in Eqs. 10 and 11 were further validated experimentally. The glycerol conversion and lactic acid yield obtained from experimental data were compared with the simulated model. The comparison results between the experimental and simulated glycerol conversion and lactic acid yield data obtained from the model developed at different temperatures are presented in Figs. 8 and 9, respectively. In general, the glycerol conversion profiles in Fig. 8 demonstrated good agreement between the experimental and simulated data across different reaction temperatures with R^2 values greater than 0.9, except for the reaction temperature of 250 °C.

Furthermore, it was noteworthy to mention that Eq. 10 exhibited improved accuracy when applied to higher reaction temperature ranges, specifically to temperatures of

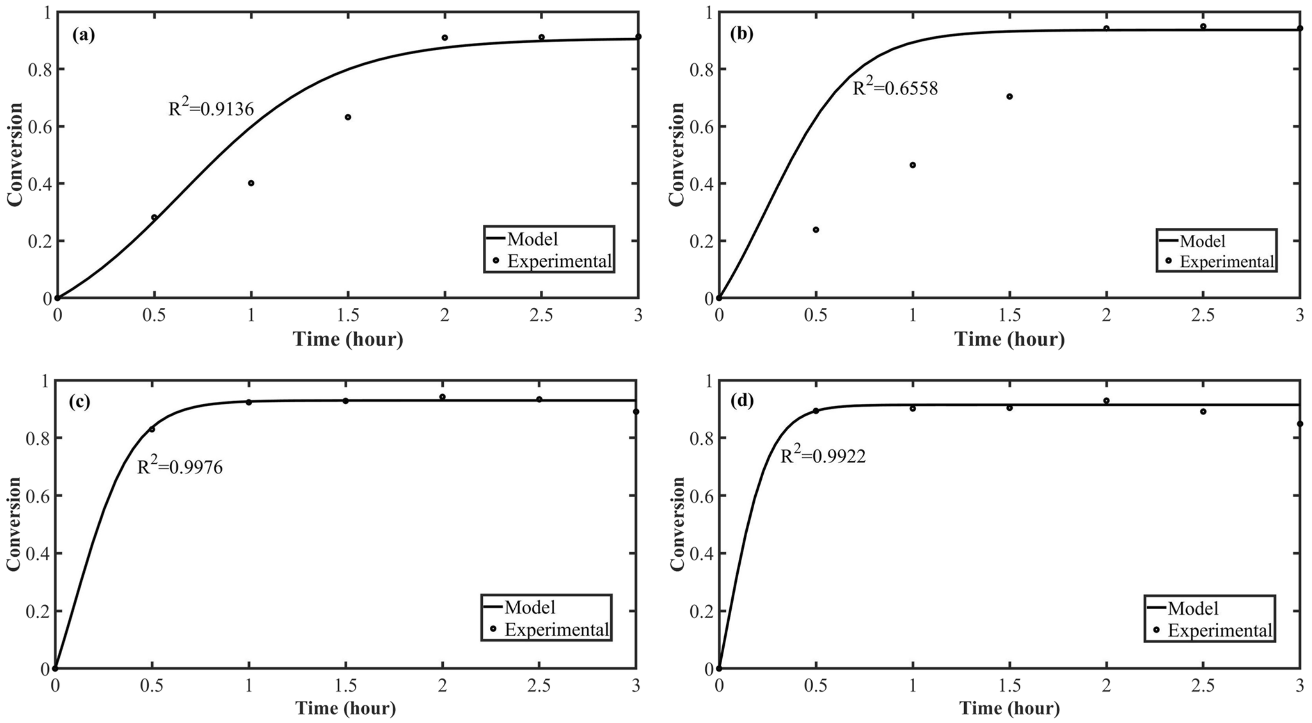

Fig. 8 The comparison between the experimental and simulated glycerol conversion profiles at **a** 240 °C, **b** 250 °C, **c** 260 °C, and **d** 270 °C

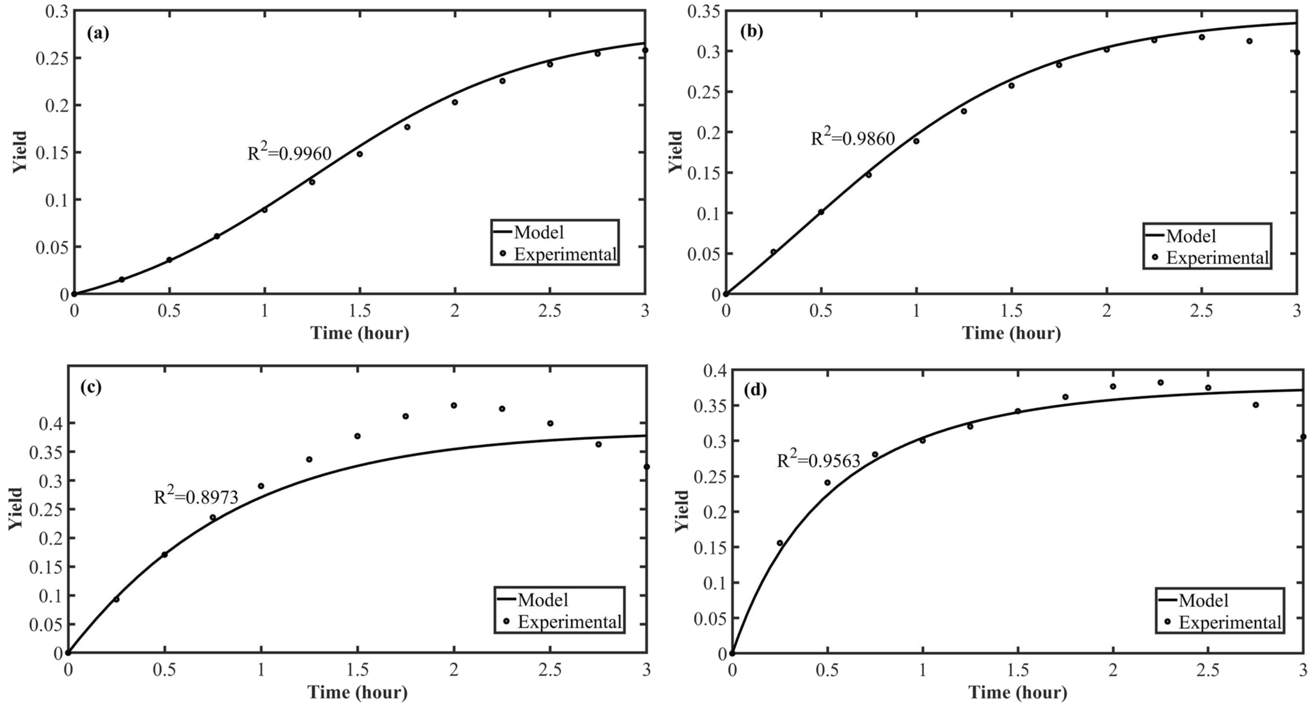

Fig. 9 The comparison between the experimental and simulated lactic acid yield profiles at: **a** 240 °C, **b** 250 °C, **c** 260 °C, and **d** 270 °C

260 °C and 270 °C. This proved that selective glycerol oxidation to lactic acid had multiple empirical models that effectively depicted its behavior at varying temperatures. This is because, at different temperature ranges, the reaction could proceed via different catalytic pathways, needing separate empirical models to precisely represent the pattern within each temperature regime. Interestingly, this observation was consistent with the findings reported by Taylor and his co-workers [67], who conducted a design of experiments (DOE) analysis and concluded that the squared temperature term in the model indicated a more pronounced impact on the response at elevated temperatures compared to lower temperatures.

Meanwhile, the profiles of lactic acid yield in Fig. 9 demonstrated a good agreement between the experimental and simulated lactic acid yield at all reaction temperatures with R^2 values between 0.9 and 1. Thus, it could be deduced that the validated model, Eq. 10, established in this study was capable of satisfactorily predicting glycerol conversion at reaction temperatures of 260 °C and 270 °C, while Eq. 11 exhibited the capability to accurately predict lactic acid yield within the reaction temperatures of 240 °C to 270 °C.

Kinetic Analysis

The kinetic parameters for selective glycerol oxidation to lactic acid at different temperatures were determined by plotting the glycerol conversions over time using linear regression analysis. The estimated specific rate constant values for each reaction temperature are presented in Table 4. The obtained rate constant values at different temperatures exhibited an increasing trend with increasing temperatures. Another research group also reported the same trend in rate constant values [25].

Moreover, the pre-exponential factor, *A*, and reaction activation energy, E_a, were calculated using the linear regression method following Eq. 8. The linearized Arrhenius equation plot is shown in Fig. 10. Hence, according to Fig. 10, the *A* and E_a values obtained were 7.002×10^{15} and 165.3 kJ/mol, respectively, with good with a reliably good R^2 value of 0.94.

Thus, the overall reaction kinetics can be expressed as follows:

$$-r_{Gly} = 7.002 \times 10^{15} exp\left(\frac{-165299}{8.3142T}\right) {C_{Gly}}^2 \tag{12}$$

Furthermore, The activation energies for NaOH [8], CaO [7], Pt/C in the presence of H_2 gas [62], Pt/C [62], Cu(16)/

Table 4 The estimated rate constant values at different temperatures

Temperature (°C)	Estimated specific rate constant, $k_s (1/M.hr)$
240	0.0953
250	0.2151
260	0.6129
270	0.7192

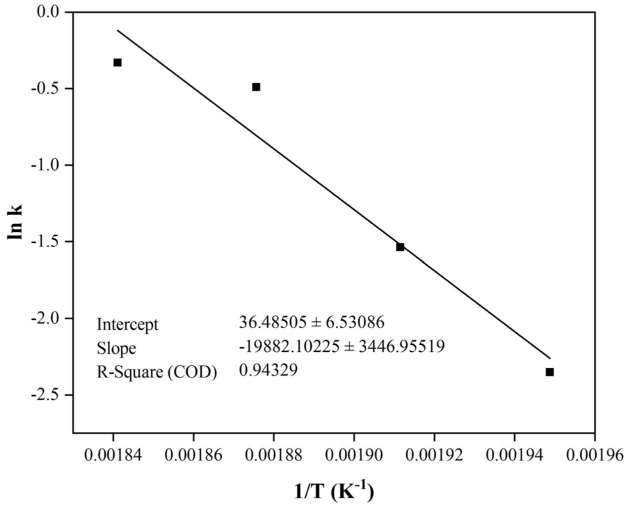

Fig. 10 Linearized Arrhenius equation plot

HAP [11], and Ni/graphite [25] catalysts were reported as 174 kJ/mol, 103 kJ/mol, 53 kJ/mol, 64 kJ/mol, 117.2 kJ/mol, and 69.2 kJ/mol, respectively. Despite the slightly higher activation energy reported in this study compared to some of the previous works, it was important to acknowledge that the initial glycerol concentration (13.23 M) used in this study was significantly higher than those reported earlier (0.33–1.10 M), which could contribute to an increased energy barrier. Moreover, it was also worth considering the influence of alkaline concentrations and reaction temperatures on the activation energy as additional contributing factors. All prior works employed alkaline media alongside the catalysts. Besides, the conversion profiles of glycerol at four different reaction temperatures are presented in Fig. 11, illustrating a comparison between the experimental and simulated results.

The SSE values of the kinetic model fitting for the reaction temperatures of 240 °C, 250 °C, 260 °C, and 270 °C, were 0.1349, 0.1321, 0.067, and 0.0244 respectively. A significantly higher SSE for lower reaction temperatures indicated a poorer fit, indicating larger discrepancies between the predicted data and experimental data. Thus, the reduced SSE observed at reaction temperatures of 260 °C, and 270 °C indicated an improved fit of the model to the experimental data at those temperatures. In short, this revealed that the pseudo-second-order kinetic model was appropriate for the evaluation of selective glycerol oxidation reaction, especially at higher reaction temperature ranges.

Conclusion

The $Ce_{1-x}Zr_xO_2$/SBA-15 catalyst exhibited excellent tolerance to high metal loadings, accommodating up to 40 wt% without experiencing significant reductions in surface area

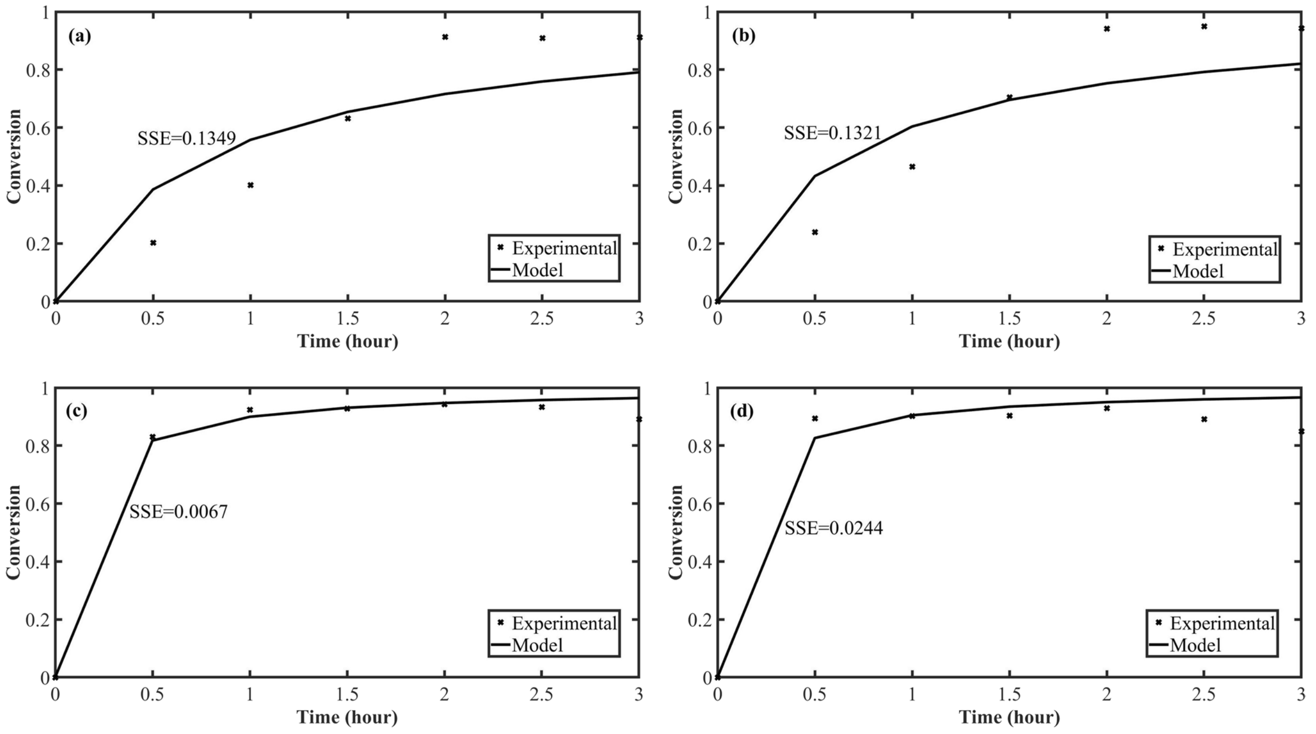

Fig. 11 The comparison between the experimental and simulated glycerol conversion profiles at **a** 240 °C, **b** 250 °C, **c** 260 °C, and **d** 270 °C

and porosity. The $10Ce_{1-x}Zr_xO_2$/SBA-15 catalyst outperformed all other synthesized catalysts, demonstrating the best catalytic performance, achieving a glycerol conversion of 93.2% and a lactic acid yield of 41.1%. Besides, the selective glycerol oxidation reaction was thoroughly examined. The study involved investigating various reaction conditions, including different catalyst loadings, reaction temperatures, and reaction times. A catalyst-to-glycerol loading of 15 wt%, a reaction temperature of 260 °C, and a reaction time of 2 h were determined to be the best reaction conditions. Excellent catalytic performance, with a high glycerol conversion of 94.2% and a 45.3% lactic acid yield was demonstrated by the $10Ce_{1-x}Zr_xO_2$/SBA-15 catalyst. The combined role of ordered mesoporosity and the specific roles of the active sites, that is the synergism created by the $Ce_{1-x}Zr_xO_2$ compounds, made it possible for the conversion of a high concentration of glycerol. Thus, precise control of the reaction conditions was crucial in facilitating the predominant occurrence of the desired reaction pathway, resulting in the selective synthesis of lactic acid. This concludes that the accelerated formation of aldehyde intermediates under these conditions was subsequently supported by a sufficiently fast hydration reaction to form lactic acid.

Furthermore, an empirical process model for both glycerol conversion and lactic acid yield was successfully modeled as a function of temperature using a second-order polynomial equation. The selective glycerol oxidation reaction to lactic acid using $10Ce_{1-x}Zr_xO_2$/SBA-15 catalyst involved mixed multiple and consecutive reactions, which involved pseudo-second-order kinetics. The $10Ce_{1-x}Zr_xO_2$/SBA-15 catalyst exhibited a comparable activation energy of 165.3 kJ/mol when compared to previously published works. In short, the developed overall reaction kinetic model was highly reliable in predicting the selective glycerol-to-lactic acid oxidation reaction very well, especially at higher reaction temperatures ($T > 260$ °C). Thus, this work provides an enhancement to previous approaches to reaction modeling and enhances the predictability of glycerol-to-lactic acid oxidation reactions. In short, at a reaction temperature of 260 °C, the $10Ce_{1-x}Zr_xO_2$/SBA-15 catalyst could successfully catalyze the selective glycerol-to-lactic acid oxidation with high glycerol conversion and lactic acid yield in only 2 h of reaction.

Acknowledgements This research work is fully funded by the Ministry of Higher Education Malaysia under the Fundamental Research Grant Scheme (FRGS/1/2021/TK0/USM/01/2).

Funding This work was supported by Ministry of Higher Education Malaysia Grant No. [FRGS/1/2021/TK0/USM/01/2].

Data Availability Enquiries about data availability should be directed to the authors.

Declarations

Conflict of interest The authors have not disclosed any competing interests.

References

1. Okoye, P., Abdullah, A.Z., Hameed, B.H.: Glycerol carbonate synthesis from glycerol and dimethyl carbonate using trisodium phosphate. J. Taiwan Inst. Chem. Eng. **68**, 51–58 (2016). https://doi.org/10.1016/j.jtice.2016.09.011
2. Kant, A., He, Y., Jawad, A., Li, X., Rezaei, F., Smith, J.D., Rownaghi, A.A.: Hydrogenolysis of glycerol over Ni, Cu, Zn, and Zr supported on H-beta. Chem. Eng. J. **317**, 1–8 (2017). https://doi.org/10.1016/j.cej.2017.02.064
3. Boz, I., Safak Boroglu, M., Zengin, Y., Kaya, B.: WO_3-based porous MCM-48 catalysts for renewable acrolein synthesis by the dehydration of glycerol. Inorg. Chem. Commun. **147**, 110240 (2023). https://doi.org/10.1016/j.inoche.2022.110240
4. Abdullah, A., Zuhairi, A., Ahmed, M., Khan, J., Shahadat, M., Umar, K., Alim, A.: A review on recent developments and progress in sustainable acrolein production through catalytic dehydration of bio-renewable glycerol. J. Clean. Prod. **341**, 130876 (2022). https://doi.org/10.1016/j.jclepro.2022.130876
5. Ahmad, M.Y., Basir, N.I., Abdullah, A.Z.: A review on one-pot synthesis of acrylic acid from glycerol on bi-functional catalysts. J. Ind. Eng. Chem. **93**, 216–227 (2020). https://doi.org/10.1016/j.jiec.2020.09.026
6. Kabwe, F.B., Zhong, J.Q., Huang, W.J., Li, C.J., Zhou, C.H.: Unveiling the contribution of Mo, V and W oxides to coking in catalytic glycerol oxidehydration. Mol. Catal. **516**, 111969 (2021). https://doi.org/10.1016/j.mcat.2021.111969
7. Chen, L., Ren, S., Ye, X.P.: Glycerol conversion to lactic acid with sodium hydroxide as a homogeneous catalyst in a fed-batch reactor. React. Kinet. Mech. Catal. **114**, 93–108 (2015). https://doi.org/10.1007/s11144-014-0786-z
8. Kishida, H., Jin, F.M., Zhou, Z.Y., Moriya, T., Enomoto, H.: Conversion of glycerin into lactic acid by alkaline hydrothermal reaction. Chem. Lett. **34**, 1560–1561 (2005). https://doi.org/10.1246/cl.2005.1560
9. Ramírez-López, C.A., Ochoa-Gómez, J.R., Fernández-Santos, M., Gómez-Jiménez-Aberasturi, O., Alonso-Vicario, A., Torrecilla-Soria, J.J.: Synthesis of lactic acid by alkaline hydrothermal conversion of glycerol at high glycerol concentration. Ind. Eng. Chem. Res. **49**, 6270–6278 (2010). https://doi.org/10.1021/ie1001586
10. Shen, Z., Jin, F., Zhang, Y., Wu, B., Kishita, A., Tohji, K., Kishida, H.: Effect of alkaline catalysts on hydrothermal conversion of glycerin into lactic acid. Ind. Eng. Chem. Res. **48**, 8920–8925 (2009). https://doi.org/10.1021/ie900937d
11. Yin, H., Zhang, C., Yin, H., Gao, D., Shen, L., Wang, A.: Hydrothermal conversion of glycerol to lactic acid catalyzed by Cu/hydroxyapatite, Cu/MgO, and Cu/ZrO_2 and reaction kinetics. Chem. Eng. J. **288**, 332–343 (2016). https://doi.org/10.1016/j.cej.2015.12.010
12. Bruno, A.M., Chagas, C.A., Souza, M.M.V.M., Manfro, R.L.: Lactic acid production from glycerol in alkaline medium using Pt-based catalysts in continuous flow reaction system. Renew. Energy **118**, 160–171 (2018). https://doi.org/10.1016/j.renene.2017.11.014
13. Qiu, L., Yin, H., Yin, H., Wang, A.: Catalytic conversion of glycerol to lactic acid over hydroxyapatite-supported metallic Ni^0 nanoparticles. J. Nanosci. Nanotechnol. **18**, 4734–4745 (2018). https://doi.org/10.1166/jnn.2018.15327

14. Shen, L., Yu, Z., Zhang, D., Yin, H., Wang, C., Wang, A.: Glycerol valorization to lactic acid catalyzed by hydroxyapatite-supported palladium particles. J. Chem. Technol. Biotechnol. **94**, 204–215 (2019). https://doi.org/10.1002/jctb.5765
15. Jiang, Z., Zhang, Z., Wu, T., Zhang, P., Song, J., Xie, C., Han, B.: Efficient generation of lactic acid from glycerol over a Ru–Zn–Cu^{I}/hydroxyapatite catalyst. Chem.— An Asian J. **12**, 1598–1604 (2017). https://doi.org/10.1002/asia.201700412
16. Moreira, A.B.F., Bruno, A.M., Souza, M.M.V.M., Manfro, R.L.: Continuous production of lactic acid from glycerol in alkaline medium using supported copper catalysts. Fuel Process. Technol. **144**, 170–180 (2016). https://doi.org/10.1016/j.fuproc.2015.12.025
17. Razali, N., Zuhairi, A.: General Production of lactic acid from glycerol via chemical conversion using solid catalyst : a review. Appl. Catal. A **543**, 234–246 (2017). https://doi.org/10.1016/j.apcata.2017.07.002
18. Abdullah, R., Saleh, S.N.M.: Embong, K, Recent developments and potential advancement in the kinetics of catalytic oxidation of glycerol. Chem. Eng. Commun. **207**, 1298–1328 (2019). https://doi.org/10.1080/00986445.2019.1641699
19. Sharninghausen, L.S., Campos, J., Manas, M.G., Crabtree, R.H.: Efficient selective and atom economic catalytic conversion of glycerol to lactic acid. Nat. Commun. **5**, 5084 (2014). https://doi.org/10.1038/ncomms6084
20. Esipovich, A.L., Zlobin, S.Y., Shirshin, K.K., Zavrazhnov, S.A., Markov, A.N.: Catalytic conversion of glycerol to lactic acid over Cu-based catalysts. Catalysts **14**, 231 (2024). https://doi.org/10.3390/catal14040231
21. Li, S., Li, S., Wang, Y., Tang, C., Qiu, L., Yu, S.: Selective Oxidation of glycerol to lactic acid catalyzed by CuO/activated carbon and reaction kinetics. ACS Omega **9**, 10583–10591 (2024). https://doi.org/10.1021/acsomega.3c08845
22. Tang, C., Li, S., Li, S., Wang, Y., Yu, S.: Selective catalytic conversion of glycerol to lactic acid over CuO–NiO complex oxides. Mol. Catal. **553**, 113804 (2024). https://doi.org/10.1016/j.mcat.2023.113804
23. Ten, S.A., Kurmanova, M.D., Kurmanbayeva, K., Torbina, V.V., Stonkus, O.A., Vodyankina, O.V.: Base-free cascade glycerol conversion to lactic acid over Pd–Bi nanoparticles immobilized in metal-organic framework Zr–UiO-66. Appl. Catal. A Gen. **674**, 119603 (2024). https://doi.org/10.1016/j.apcata.2024.119603
24. Akbulut, D., Özkar, S.: A review of the catalytic conversion of glycerol to lactic acid in the presence of aqueous base. RSC Adv. **12**, 18864–18883 (2022). https://doi.org/10.1039/d2ra03085c
25. Yin, H., Yin, H., Wang, A., Shen, L.: Catalytic conversion of glycerol to lactic acid over graphite-supported nickel nanoparticles and reaction kinetics. J. Ind. Eng. Chem. **57**, 226–235 (2018). https://doi.org/10.1016/j.jiec.2017.08.028
26. Yin, H., Yin, H., Wang, A., Shen, L., Liu, Y., Zheng, Y.: Catalytic conversion of glycerol to lactic acid over metallic copper nanoparticles and reaction kinetics. J. Nanosci. Nanotechnol. **17**, 1255–1266 (2017). https://doi.org/10.1166/jnn.2017.12573
27. Saleh, S.N.M., Abdullah, A.Z.: Zirconium-cerium oxides supported on SBA-15 as catalyst for shape-selective synthesis of lactic acid from glycerol. Waste Biomass Valor. **12**, 2565–2578 (2020). https://doi.org/10.1007/s12649-020-01200-4
28. Liao, Y., Fu, M., Chen, L., Wu, J., Huang, B., Ye, D.: Catalytic oxidation of toluene over nanorod-structured Mn–Ce mixed oxides. Catal. Today **216**, 220–228 (2013). https://doi.org/10.1016/j.cattod.2013.06.017
29. Abdullah, A.Z., Razali, N., Lee, K.T.: Optimization of K/SBA-15 catalyzed transesterification of palm oil using response surface methodology. Fuel Process. Technol. **90**, 958–964 (2009). https://doi.org/10.1016/j.fuproc.2009.03.023
30. Abdullah, A.Z., Yaacob, M.H., Basir, N.I.: Synergy between oxides of Ni and Ca for selective catalytic lactic acid synthesis from glycerol in a single step process. J. Ind. Eng. Chem. **85**, 282–288 (2020). https://doi.org/10.1016/j.jiec.2020.02.011
31. Abdullah, N., Ainirazali, N., Ellapan, H.: Structural effect of Ni/SBA-15 by Zr promoter for H_2 production via methane dry reforming. Int. J. Hydrogen Energy **46**, 24806–24813 (2021). https://doi.org/10.1016/j.ijhydene.2020.07.060
32. Thanasilp, S., Schwank, J.W., Meeyoo, V., Pengpanich, S., Hunsom, M.: One-pot oxydehydration of glycerol to value-added compounds over metal-doped SiW/HZSM-5 catalysts: effect of metal type and loading. Chem. Eng. J. **275**, 113–124 (2015). https://doi.org/10.1016/j.cej.2015.04.010
33. Marques, F.L., Oliveira, A.C., Filho, J.M., Rodríguez-Castellón, E., Cavalcante, C.L., Vieira, R.S.: Synthesis of lactic acid from glycerol using a Pd/C catalyst. Fuel Process. Technol. **138**, 228–235 (2015). https://doi.org/10.1016/j.fuproc.2015.05.032
34. Zhang, C., Wang, T., Liu, X., Ding, Y.: Selective oxidation of glycerol to lactic acid over activated carbon supported Pt catalyst in alkaline solution. Chinese J. Catal. **37**, 502–509 (2016). https://doi.org/10.1016/S1872-2067(15)61055-5
35. Zhang, C., Wang, T., Liu, X., Ding, Y.: Cu-promoted Pt/activated carbon catalyst for glycerol oxidation to lactic acid. Mol. Catal. A Chem. **424**, 91–97 (2016). https://doi.org/10.1016/j.molcata.2016.08.018
36. Feng, Y., Yin, H., Wang, A., Gao, D., Zhu, X., Shen, L., Meng, M.: Selective oxidation of 1,2-propanediol to lactic acid catalyzed by nanosized $Mg(OH)_2$-supported bimetallic Au-Pd catalysts. Appl Catal. A, Gen. **482**, 49–60 (2014). https://doi.org/10.1016/j.apcata.2014.05.022
37. Shen, Y., Zhang, S., Li, H., Ren, Y., Liu, H.: Efficient synthesis of lactic acid by aerobic oxidation of glycerol on Au-Pt/TiO_2 catalysts. Chem. A Eur. J. **16**, 7368–7371 (2010). https://doi.org/10.1002/chem.201000740
38. Yan, H., Qin, H., Feng, X., Jin, X., Liang, W., Sheng, N., Zhu, C., Wang, H., Yin, B., Liu, Y., Chen, X., Yang, C.: Synergistic Pt/MgO/SBA-15 nanocatalysts for glycerol oxidation in base-free medium : Catalyst design and mechanistic study. J. Catal. **370**, 434–446 (2019). https://doi.org/10.1016/j.jcat.2019.01.015
39. Nara, T.Y., Togashi, H., Ono, S., Egami, M., Sekikawa, C., Suzuki, Y.H., Masuda, I., Ogawa, J., Horinouchi, N., Shimizu, S., Mizukami, F., Tsunoda, T.: Improvement of aldehyde tolerance and sequential aldol condensation activity of deoxyriboaldolase via immobilization on interparticle pore type mesoporous silica. J. Mol. Catal. B Enzym. **68**, 181–186 (2011). https://doi.org/10.1016/j.molcatb.2010.10.008
40. Zhong, X., Barbier, J., Duprez, D., Zhang, H., Royer, S.: Modulating the copper oxide morphology and accessibility by using micro-/mesoporous SBA-15 structures as host support: effect on the activity for the CWPO of phenol reaction. Appl. Catal. B Environ. **121–122**, 123–134 (2012). https://doi.org/10.1016/j.apcatb.2012.04.002
41. Hoo, P.Y., Abdullah, A.Z.: Direct synthesis of mesoporous 12-tungstophosphoric acid SBA-15 catalyst for selective esterification of glycerol and lauric acid to monolaurate. Chem. Eng. J. **250**, 274–287 (2014). https://doi.org/10.1016/j.cej.2014.04.016
42. Rivoira, L.P., Valles, V.A., Martínez, M.L., Sa-ngasaeng, Y., Jongpatiwut, S., Beltramone, A.R.: Catalytic oxidation of sulfur compounds over Ce-SBA-15 and Ce–Zr-SBA-15. Catal. Today **360**, 116–128 (2021). https://doi.org/10.1016/j.cattod.2019.08.005
43. Saleh, S.N.M., Yusoff, M.H.M., Abdullah, A.Z.: Caesium salt of tungstophosphoric acid supported on mesoporous SBA-15 Catalyst for selective esterification of lauric acid with glycerol to monolaurin. Arab. J. Sci. Eng. **43**, 5771–5783 (2018). https://doi.org/10.1007/s13369-017-3009-x

44. Bhange, P., Bhange, D.S., Pradhan, S., Ramaswamy, V.: Direct synthesis of well-ordered mesoporous Al-SBA-15 and its correlation with the catalytic activity. Appl. Catal. A-Gen. **400**, 176–184 (2011). https://doi.org/10.1016/j.apcata.2011.04.031
45. Arcanjo, M.R.A., Silva, I.J., Rodríguez-Castellón, E., Infantes-Molina, A., Vieira, R.S.: Conversion of glycerol into lactic acid using Pd or Pt supported on carbon as catalyst. Catal. Today **279**, 317–326 (2015). https://doi.org/10.1016/j.cattod.2016.02.015
46. Purushothaman, R.K.P., van Haveren, J., van Es, D.S., Melián-Cabrera, I., Meeldijk, J.D., Heeres, H.J.: An efficient one-pot conversion of glycerol to lactic acid using bimetallic gold-platinum catalysts on a nanocrystalline CeO_2 support. Appl. Catal. B **147**, 92–100 (2014). https://doi.org/10.1016/j.apcatb.2013.07.068
47. Chen, Y., Zhang, X.L., Chen, X., Dong, B.B., Zheng, X.C.: MCM-41 supported 12-tungstophosphoric acid mesoporous materials: preparation, characterization, and catalytic activities for benzaldehyde oxidation with H_2O_2. Solid State Sci. **24**, 21–25 (2013). https://doi.org/10.1016/j.solidstatesciences.2013.06.017
48. Tao, M., Sun, N., Li, Y., Tong, T., Wielicako, M., Wang, S., Wang, X.: Heteropolyacids embedded in a lipid bilayer covalently bonded to graphene oxide for the facile one-pot conversion of glycerol to lactic acid. J. Mater. Chem. A **5**, 8325–8333 (2017). https://doi.org/10.1039/c7ta01334e
49. Pistonesi, C., Juan, A., Irigoyen, B., Amadeo, N.: Theoretical and experimental study of methane steam reforming reactions over nickel catalyst. Appl. Surf. Sci. **253**, 4427–4437 (2007). https://doi.org/10.1016/j.apsusc.2006.09.054
50. Farahmandjou, M., Farahmandjou, M., Zarinkamar, M., Firoozabadi, T.P.: Synthesis of Cerium Oxide (CeO2) nanoparticles using simple CO-precipitation method. Rev. Mex. Física **62**, 496–499 (2016)
51. Horti, N.C., Kamatagi, M.D., Nataraj, S.K., Wari, M.N., Inamdar, S.R.: Structural and optical properties of zirconium oxide (ZrO_2) nanoparticles: effect of calcination temperature. Nano Express **1**, 010022 (2020). https://doi.org/10.1088/2632-959X/ab8684
52. Philip, J.T., Koshy, C.P., Mathew, M.D.: Advanced characterization of precipitation synthesized ceria and ceria-zirconia hybrid nanoparticles. Mater. Res. Express **6**, 1150e1 (2019). https://doi.org/10.1088/2053-1591/ab4fd5
53. Gagea, B.C., Lorgouilloux, Y., Altintas, Y., Jacobs, P.A., Martens, J.A.: Bifunctional conversion of n-decane over HPW heteropoly acid incorporated into SBA-15 during synthesis. J. Catal. **265**, 99–108 (2009). https://doi.org/10.1016/j.jcat.2009.04.017
54. Embong, K., Basir, N.I., Abdullah, A.Z.: Selective conversion of glycerol to lactic acid by CaO/γ–Al_2O_3 supported catalyst. J. Eng. Sci. **16**, 29–45 (2020). https://doi.org/10.21315/jes2020.16.1.3
55. Bruno, A.M., Simões, T.D.R., Souza, M.M.V.M., Manfro, R.L.: Cu catalysts supported on CaO/MgO for glycerol conversion to lactic acid in alkaline medium employing a continuous flow reaction system. RSC Adv. **10**, 31123–31138 (2020). https://doi.org/10.1039/d0ra06547a
56. Liu, P., Derchi, M., Hensen, E.J.M.: Promotional effect of transition metal doping on the basicity and activity of calcined hydrotalcite catalysts for glycerol carbonate synthesis. Appl. Catal. B Environ. **144**, 135–143 (2014). https://doi.org/10.1016/j.apcatb.2013.07.010
57. Lakshmanan, P., Upare, P.P., Le, N.T., Hwang, Y.K., Hwang, D.W., Lee, U.H., Kim, H.R., Chang, J.S.: Facile synthesis of CeO_2-supported gold nanoparticle catalysts for selective oxidation of glycerol into lactic acid. Appl. Catal. A-Gen. **468**, 260–268 (2013). https://doi.org/10.1016/j.apcata.2013.08.048
58. Feng, S., Takahashi, K., Miura, H., Shishido, T.: One-pot synthesis of lactic acid from glycerol over a Pt/L-Nb_2O_5 catalyst under base-free conditions. Fuel Process. Technol. **197**, 106202 (2020). https://doi.org/10.1016/j.fuproc.2019.106202
59. Maris, E.P., Ketchie, W.C., Murayama, M., Davis, R.J.: Glycerol hydrogenolysis on carbon-supported PtRu and AuRu bimetallic catalysts. J. Catal. **251**, 281–294 (2007). https://doi.org/10.1016/j.jcat.2007.08.007
60. Kulkarni, R.M., Britto, P.J., Narula, A., Saqline, S., Anand, D., Bhagyalakshmi, C., Herle, R.N.: Kinetic studies on the synthesis of fuel additives from glycerol using CeO_2-ZrO_2 metal oxide catalyst. Biofuel Res. J. **7**, 1100–1108 (2020). https://doi.org/10.18331/BRJ2020.7.1.2
61. Xiu, Z., Wang, H., Cai, C., Li, C., Yan, L., Wang, C., Li, W., Xin, H., Zhu, C., Zhang, Q., Liu, Q., Ma, L.: Ultrafast glycerol conversion to lactic acid over magnetically recoverable Ni–NiO_x@C catalysts. Ind. Eng. Chem. Res. **59**, 9912–9925 (2020). https://doi.org/10.1021/acs.iecr.0c01145
62. Kulkarni, R.M., Arvind, N.: Acetalization of glycerol and benzaldehyde to synthesize biofuel additives using SO_4^{2-}/CeO_2–ZrO_2 catalyst. Heliyon **7**, 1–9 (2021). https://doi.org/10.1016/j.heliyon.2021.e06018
63. Albuquerque, E.M., Borges, L.E.P., Fraga, M.A.: Lactic acid production from aqueous-phase selective oxidation of hydroxyacetone. J. Molec. Catal. A Chem. **400**, 64–70 (2015). https://doi.org/10.1016/j.molcata.2015.02.005
64. Palacio, R., López, D., Hernández, D.: Bimetallic AuCu nanoparticles supported on CeO_2 as selective catalysts for glycerol conversion to lactic acid in aqueous basic medium. J. Nanoparticle Res. (2019). https://doi.org/10.1007/s11051-019-4594-2
65. Palacio, R., Sebastian, T., Sébastien, R., Anne, S.M., Diana, L., Hernándeza, D.: CuO/CeO_2 catalysts for glycerol selective conversion to lactic acid. Dalt. Trans. **47**, 4572–4582 (2018). https://doi.org/10.1039/c7dt04340f
66. Palacio, R., Torres, S., Lopez, D., Hernandez, D.: Selective glycerol conversion to lactic acid on Co_3O_4/CeO_2 catalysts. Catal. Today **302**, 196–202 (2018). https://doi.org/10.1016/j.cattod.2017.05.053
67. Taylor, C.J., Pomberger, A., Felton, K.C., Grainger, R., Barecka, M., Chamberlain, T.W., Bourne, R.A., Johnson, C.N., Lapkin, A.A.: A brief introduction to chemical reaction optimization. Chem. Rev. (2023). https://doi.org/10.1021/acs.chemrev.2c00798

Authors and Affiliations

Syamima Nasrin Mohamed Saleh[1] · **Fakhrony Sholahudin Rohman**[1] · **Anwar Ul-Hamid**[2] · **Ahmad Zuhairi Abdullah**[1]

✉ Ahmad Zuhairi Abdullah
chzuhairi@usm.my

[1] School of Chemical Engineering, Universiti Sains Malaysia, Engineering Campus, 14300 Nibong Tebal, Pulau Pinang, Malaysia

[2] Core Research Facilities, King Fahd University of Petroleum & Minerals, Dhahran 31261, Saudi Arabia